THESIS FOR THE DEGREE OF LICENTIATE OF PHYSICS

# Correlation effects in ionic perovskite crystals

Konstantinos Papadopoulos

Department of Physics
*Division of Material Physics*
Chalmers University of Technology
Gothenburg, Sweden 2022

Correlation effects in ionic perovskite crystals
KONSTANTINOS PAPADOPOULOS

© KONSTANTINOS PAPADOPOULOS, 2022.

Department of Physics
Chalmers University of Technology
SE-412 96 Gothenburg
Sweden
Telephone +46 (0)31 772 1000

This work was funded by the Swedish Research Council (VR) through a Starting Grant (Dnr. 2017-05078) and the Area of Advance-Materials Science of Chalmers University of Technology.

Printed by Chalmers Reproservice
Gothenburg, Sweden 2022

# Abstract

In the field of spintronics and optoelectronics we focus on the understanding and manipulation of interactions between electron charges, electron spins and photons. These entities can be used as information or charge carriers in spintronic and optoelectronic devices, depending on the conducting/insulating and magnetic properties of the implemented physical systems. We are interested in multifunctional materials with strongly correlated physical entities, which present a wide range of electronic and magnetic properties. Nevertheless, this richness of physical qualities is often a result of very complex, dynamic systems. The behaviour of these materials cannot be fully described unless we examine microscopically the sources and evolution of electric and magnetic interactions.

A typical example of correlated systems are perovskite materials. During a 70 year long research, interest in these systems has been growing exponentially as new properties emerge and our understanding of the circumstances that enable them deepens. Perovskites are structurally flexible and can host most of the elements in the periodic table. As a result they can behave as conductors, superconductors, semiconductors or insulators. This wide repertoire gives them a prominent role in spintronics and optoelectronics.

This thesis focuses on perovskite materials from two different families, aiming to understand how structural and chemical characteristics affect the magnetic and electronic properties of these systems. Our studies are primarily based on muon spectroscopy, a technique that can probe the spatial magnetic field distributions in our samples as a function of applied field and temperature. First, we investigate the magnetic structure of the polycrystaline double perovskite oxides $LaSr_{1-x}Ca_xNiReO_6$ for x=0,1. A succession of magnetic phases has been identified in both compounds. Below $T_c$=23 K for x=0 and $T_c$=103 K for x=1, a ferrimagnetically ordered phase appears. Above their $T_c$ both compounds go through a dense and a dilute magnetic phase before paramagnetism takes over at T>250 K.

On a different note, we focused on ion dynamics in the hybrid organic/inorganic perovskite single crystals $(CH_3NH_3)PbX_3$ where X=Br, Cl. These samples are part of the hybrid perovskite class of promising solar cell materials. Muon spectroscopy allows us to study the kinetics of ions, which affect the stability of the solar cells and the efficiency of charge carrier diffusion. Measurements were carried out in the 30-340 K temperature range, in the dark and under illumination. As temperature rises and the crystals undergo multiple structural transitions, the dark/light environments supress or enhance the fluctuations of the organic molecule and the diffusion of the two halides.

The results of our studies provide an insight to how the correlations between structure and interactions of ionic lattices influence the macroscopic properties. The process of understanding these correlations leads us closer to stable perovskite materials with well-tuned properties, increasing our potential to use natural resources evermore effectively.

**Keywords:** correlated systems, spintronics, perovskites, muon spectroscopy, magnetic order, ion dynamics, solar cells, multifunctional materials.

# List of Papers

I. Intertwined Magnetic Sub-Lattices in the Double Perovskite Compound $LaSrNiReO_6$

   Ola Kenji Forslund, Konstantinos Papadopoulos, Elisabetta Nocerino, Gerald Morris, Bassam Hitti, Donald Arseneau, Vladimir Pomjakushin, Nami Matsubara, Jean-Christophe Orain, Peter Svedlindh, Daniel Andreica, Somnath Jana, Jun Sugiyama, Martin Månsson, and Yasmine Sassa

   Physical Review B, 2020, 102.14: 144409.

II. Influence of the Magnetic Sub-Lattices in the Double Perovskite Compound $LaCaNiReO_6$

   Konstantinos Papadopoulos, Ola Kenji Forslund, Elisabetta Nocerino, Fredrik O.L. Johansson, Gediminas Simutis, Nami Matsubara, Gerald Morris, Bassam Hitti, Donald Arseneau, Jean-Christophe Orain, Vladimir Pomjakushin, Peter Svedlindh, Daniel Andreica, Lars Börjesson, Jun Sugiyama, Martin Månsson and Yasmine Sassa

   arXiv preprint arXiv:2111.05920, 2021.

III. Photophysical dynamics in $(CH_3NH_3)PbX_3$ (X=Br, Cl) single crystal perovskites studied by Muon-Spin Spectroscopy

   Konstantinos Papadopoulos, Ola Kenji Forslund, Elisabetta Nocerino, Nami Matsubara, P.K. Nayak, S. P. Cottrell, Lars Börjesson, Jun Sugiyama, Martin Månsson, and Yasmine Sassa

   Manuscript

# Contribution Report

I. K.P performed the experiment, the data analysis and co-authored the manuscript.
II. K.P performed the experiment, analysed the data and wrote the manuscript.
III. K.P performed the experiment and analysed the data. The first draft of the manuscript was written by K.P and O.K.F.

# Table of Contents

**1 Introduction** **1**

**2 Magnetic models and interactions** **3**
2.1 Magnetism in atoms . . . . . 3
2.2 Exchange interactions . . . . . 6
2.3 Magnetism in solids . . . . . 6
2.4 Geometrical frustration . . . . . 7

**3 Perovskites** **9**
3.1 Double Perovskite Oxides . . . . . 9
3.2 Organometallic Perovskite Halides . . . . . 11

**4 Muon spectroscopy ($\mu^+$SR)** **13**
4.1 The life of a muon . . . . . 13
4.2 The muon as magnetic probe . . . . . 15
4.3 The $\mu^+$**SR** experiment . . . . . 18

**5 Results and Discussion** **21**
5.1 Magnetic phases of Ni-Re based double perovskites . . . . . 21
5.2 Ion kinetics in the hybrid methylammonium lead halide perovskites . 24

**6 Conclusions and Outlooks** **29**

**Acknowledgements** **30**

# Thesis layout

This thesis is structured into 5 chapters as follows:

**Chapter 1** sets a perspective of how fundamental research widened the range of functional materials and created new fields of research. In this context, the studied materials and experimental technique are introduced.

**Chapter 2** introduces magnetism and magnetic interactions at an atomic and solid level, in an effort to be both self-consistent and consistent with the studied systems and experimental technique which it governs.

**Chapter 3** focuses on the experimental technique and describes the nature of the probe, the interaction of the probe with a specimen and the experimental method.

**Chapter 4** summarizes the results of the listed papers.

**Chapter 5** concludes the thesis with an overview of results and open questions.

# Chapter 1

# Introduction

Modern societies have evolved into systems organized, interconnected and supported by electronic devices, while dependent on the power required for their function. Consequently the information technology and energy sectors are in the frontier of scientific research and industrial development. A crisis has been visible in the horizon in both fields for the last decades, as the conventional methods were reaching their limits and resources become ever more scarce and expensive. It is up to the scientific society to create new breakthroughs with materials and their properties, that can enhance existing technologies or even create a new generation of electronic devices.

While the electromagnetic induction was discovered by Michael Faraday and the photovoltaic effect demonstrated by Edmond Becquerel in the 1830s, it took a century and the realization of electron wave functions in the periodic potential of crystalline solids by Felix Bloch until the quantum theory of solids was established. This quantum approach gave rise to new theories and experiments that identified a very rich and complex set of interactions that exist between electron charges, electron spins and photons. Eventually in the last thirty years, the solid state physics community was confident to approach systems where these entities interact and produce a variety of physical properties. The fields of spintronics and optoelectronics were created.

During this period a wide selection of materials was synthesized and characterized in order to detect, understand and tune the desired properties. The chemical composition, dimensionality and thermodynamic state of these materials determine their properties, which are also susceptible to change when the sample's environment is altered. Even more ambitious is the search for classes of multifunctional materials which, with a chemical substitution of elements, can present a multitude of properties, even of opposite character. Such a class of materials are perovskites. Their structure allows great flexibility across the periodic table, which makes them very versatile but also complex systems. Research has shown that perovskite materials are potentially suitable for various spintronic and optoelectronic applications. However, the complex relations between the governing interactions, the structural and chemical composition responsible for their physical properties, make them a subject of intense fundamental research.

In this thesis we have studied inorganic oxide and organometallic halide perovskite materials with the powerful local probe provided by spin-polarized muons. The technique, namely muon spin rotation, relaxation or resonance ($\mu^+$SR), enables the study of samples in a neutral environment of zero applied fields. In that way, the

intrinsic properties of materials can be studied while changing one of the external stimuli at a time. Muon spins reveal the type and the evolution of magnetic field distributions in the materials. With this information we can follow the magnetic ordering or detect fluctuations and migration of species in our material. Concerning limitations, $\mu^+$SR has a specific time window and lacks element specificity, therefore should be accompanied by other experimental techniques or numerical calculations in order to construct a complete picture of the physical systems. Our two sets of perovskite materials exhibit magnetic-insulating and semiconducting behaviour respectively, for which $\mu^+$SR offers us an insight to the magnetic phases, structural phases and ion kinetics dependent on temperature, external magnetic fields and illumination.

# Chapter 2

# Magnetic models and interactions

In this chapter we lay out an overview of the interactions between magnetic moments and the effect of their magnetic, electrostatic and structural environment. We also describe the conditions under which magnetic frustration appears. This study is focused on a selection of ionic solids, probed with spin-polarized muons. Since the principle interactions in our experiments are magnetic, by displaying aspects of the micro- and macroscopic picture of interacting magnetic moments the reader will be provided with further insight into the following experimental results.

## 2.1 Magnetism in atoms

The fundamental sources of magnetism are the spin of an electron and the angular momenta created with the orbital motion of an electron around a nucleus. Classically, the magnetic dipole moment of an orbiting electron is defined as $\mu_L = -\frac{|e|}{2m}\mathbf{L}$ . From Bohr's quantum model [1, 2] we accept only integer multiples of $\hbar$ for the angular momenta (Fig. 2.1a), that leads us to $\mu_L = -\frac{|e|}{2m}\sqrt{l(l+1)}\hbar$ and its $z$ component $\mu_{Lz} = -\frac{|e|}{2m}m_l\hbar$ . For $m_l = 1$ we have the magnetic moment at the ground state, called Bohr's magneton: $\mu_B = \frac{e\hbar}{2m} = 9.27 \cdot 10^{-24} J/T$ . The intrinsic angular momentum of an electron, denoted spin, creates an equivalent magnetic moment $\mu_S = -g_0\frac{|e|}{2m}\mathbf{S}$ . The total magnetic moment of an electron can now be defined as $\mathbf{J} = \mathbf{L} + \mathbf{S}$ and its magnetic moment as $\mu_J = -g\frac{|e|}{2m}\mathbf{J}$ where $g$ a proportionality constant called the Lande factor. The total angular momentum will precess around an externally applied magnetic field $\mathbf{H}$, also with a quantized projection along the field (Fig. 2.1b). The energy contribution from the external field will be proportional to the total magnetic quantum number $m_j$, thus creating an energy splitting of the original orbitals, known as Zeeman effect [3].

Protons and neutrons of the nuclei also possess a spin. The total spin of the nucleus $\mathbf{I}$ is the vector sum of the nucleon spins. Nucleons have equivalent quantum numbers to electrons and follow a set of arrangement rules. The nuclear magnetic dipole moment is $\mu_n = -g_N\frac{|e|}{2m_P}\mathbf{I}$ and its z component $\mu_{nz} = g_n\frac{|e|}{2m_P}m_I\hbar = g_n\mu_{Bn}m_I$ ,where $m_P$ is the proton mass, $g_n$ the nuclear g-factor and $\mu_{Bn} = 5.049 \cdot 10^{-27} J/T$ the nuclear magneton, which is 2000 times smaller than the electron magneton due to the proton mass. The nuclear g-factor can attain positive or negative values which results in nuclei having a magnetic moment parallel or antiparallel to their spin, contrary to electrons where the magnetic moment is always antiparallel

to their spin.

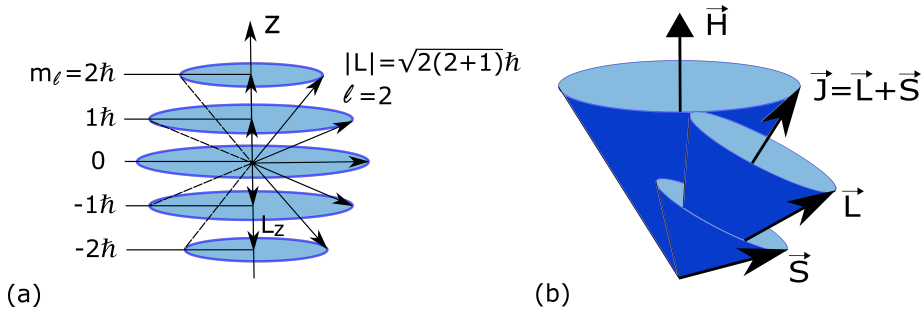


**Figure 2.1: (a):** In Bohr's model for a single electron, the orbital angular momenta will be quantized ($l$) as well as its projection along a space direction ($m_l$). From the Larmor precession, a magnetic moment is generated in multiples of the magnetic quantum number $m_l$. **(b):** In L-S coupling the orbital **L** and spin **S** angular momentum combined produce the total angular momentum **J**. When an external magnetic field is present, the projection of **J** along **H** is also quantized. The magnetic energy contribution is proportional to $J_z$. The illustrations were inspired from [4].

In the case of ions with partially filled shells, if the ions are sufficiently light so that the spin-spin and orbit-orbit coupling are stronger than the spin-orbit coupling [5], the electronic ground state can be well approximated from Hund's rules with Pauli's exclusion principle [6]. For heavier atoms, another coupling scheme, namely j-j coupling, describes electronic arrangements in better agreement with experimental results. In the j-j scheme [5], spin-orbit coupling (SOC) is the principle interaction with the form:

$$H_{LS} = -\mu_{\mathbf{s}} \cdot \mathbf{B}_l = \lambda \sum_i \mathbf{S}_i \cdot \mathbf{L}_i \tag{2.1}$$

,where $\lambda$ is the coupling constant and $\mathbf{B}_l$ the effective magnetic field generated by the orbiting electrons. In transition metal coordination complexes, additionally to the coupling of momenta, ions interact with the electrostatic environment of neighbouring ligands. The sum of these interactions at the position of each ion $\mathbf{r}$ comprises an inhomogeneous electronic field called the crystal field [7]:

$$V(\mathbf{r}) = \int \frac{\rho(\mathbf{r}')}{|\mathbf{r} - \mathbf{r}'|} d\mathbf{r}' \tag{2.2}$$

,where $\rho(\mathbf{r}')$ the charge density of the surrounding electrons. Eventually, the hamiltonian which describes an electron with orbital and spin momentum **L,S** in a magnetic field **B** is:

$$H = -\frac{\hbar^2}{2m}\nabla^2 + V_0(\mathbf{r}) + V_{cr}(\mathbf{r}) + \lambda \mathbf{L} \cdot \mathbf{S} + g_L \mu_B \mathbf{B_0} \cdot \mathbf{L} + g_s \mu_B \mathbf{B_0} \cdot \mathbf{S} \tag{2.3}$$

The first term describes the kinetic energy. The second and third term describe the potential energy of the free atom and the crystal field potential respectively. The

fourth term accounts for the spin-orbit interaction and the last two terms include the orbital and spin Zeeman interactions with the magnetic field. The competition between momentum coupling and the crystal field interaction (CF) determines the ground state. In rare earths and heavy transition metals, where SOC is larger than CF, the J is a good quantum number and Hund's third rule is valid. If CF dominates then Hund's rules cannot be applied and J is no more a good quantum number. The L-S coupling is broken up and the crystal field splitting of the L levels results in a time averaged orbital momentum $< L >= 0$. This phenomenon is known as orbital quenching and is observed in $3d$ transition metals.

In a material, most of the orbital and spin momenta are mutually cancelling. In case of uncoupled momenta though, the atoms will have a total magnetic moment. When this material is placed in a magnetic field $\mathbf{H}$, it will interact with a given energy $U = -\mu\mathbf{H}$, and be magnetized $\mathbf{M} = \frac{d\mu}{dV}$. The net magnetization is given by $\mathbf{M} = \chi\mathbf{H}$, where $\chi$ is the magnetic susceptibility of the material. For $\chi < 0$ the material resists magnetization and is called *diamagnetic*, while for $\chi > 0$, in a *paramagnetic* state, it embraces magnetization. In reality materials present a much more rich and complex magnetic behaviour with spontaneously arranged formations of magnetic moments. These magnetic states are the $ferromagnetic$, $antiferromagnetic$, $ferrimagnetic$, or variations of helical states and spin waves as presented in Figure 2.2.

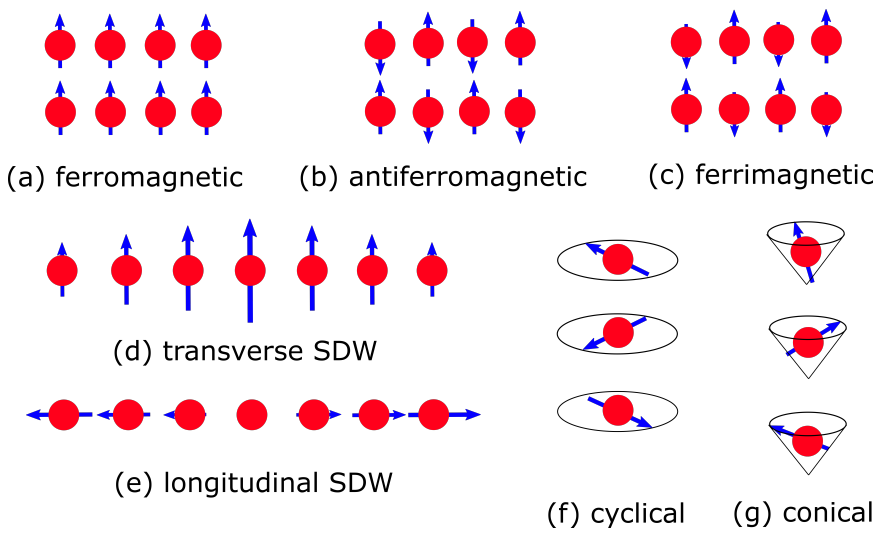


**Figure 2.2:** Different arrangements of magnetic moments lead to magnetic states with specific physical properties for materials. Ferromagnetic and ferrimagnetic materials have a spontaneous net magnetization while antiferromagnetic materials, although ordered, present no net magnetization. Cyclical or helical spin arrangements can create periodic modulations such as spin density waves (SDWs) or skyrmion quasiparticles. These illustrations were reproduced from [8].

## 2.2 Exchange interactions

The description of these magnetic states relies on our understanding of how certain magnetic ions are situated and interact within the lattice. Generally, when applying a perturbation, we consider both low and high excited ionic states. In Heisenberg's approximation the ion hamiltonian is being replaced by an effective, spin hamiltonian [9, 10] that describes accurately the low-lying states:

$$H = -\sum J_{ij}(\mathbf{s_i} \cdot \mathbf{s_j}) \tag{2.4}$$

,where $J_{ij}$ are the exchange coupling constants of the nearest neighbours. This magnetic interaction is known as direct exchange, arising from the direct Coulomb interaction between electrons of neighbouring ions. For $J > 0$ this interaction predicts ferromagnetic while for $J < 0$ antiferromagnetic ordering. A different situation in a material could be that two magnetic ions interact through an intermediate, non-magnetic ion. The length and the angle of the bonds between them create a type of interaction called superexchange. Goodenough, Kanamori and Anderson [11, 12] postulated that when the orbitals of the two magnetic ions overlap, the interaction is antiferromagnetic, while when they have a weak or zero overlap they couple ferromagnetically. A variety of exchange interactions is generally available depending on the orbital filling, localized or delocalized moments and the symmetry of interacting ions. In double exchange the electron hopping mediates a spin correlation between the neighbouring magnetic ions. The antisymmetric Dzialoshinsky-Moria exchange interactions occur when the site symmetry of interacting ions is uniaxial or lower, and forces a perpendicular alignment of spins. An RKKY indirect exchange appears between two localized core spins through an intermediate direct exchange with the spin of a conduction electron. Since Heisenberg's picture considers only electrons localized at atomic sites, the exchange between conduction electrons in itinerant electron systems is not described. Hubbard proposed a model [13] that attempts to contain both band-like and localized behaviour. In the Hubbard model, different spin exchange processes dominate depending on the relative alignment of various single particle levels.

## 2.3 Magnetism in solids

Let us now zoom out, to the bulk of the material. The most dramatic result of particle interactions is the creation of macroscopic states with collective physical properties. The creation of these states can be deduced thermodynamically from the free energy $F$ of the partition function $Z = \exp(-F/k_B T)$. At a phase transition, various physical quantities undergo substantial changes, which lead to dramatic shifts of the free energy. In the critical region, the behaviour of our system is described by a set of critical exponents. The order parameter is a statistical function that changes values at each phase. In magnetism the representative order parameter is the magnetization density:

$$m(T) = \frac{1}{V} \lim_{H \to 0} M(H,T) \propto \begin{cases} 0 & , \ T > T_C \\ H^{\frac{1}{\delta}} & , \ T = T_C \\ |t|^{\beta} & , \ T < T_C \end{cases} \tag{2.5}$$

,where $t = (T - T_C)/T_C$, the reduced temperature. The singular behaviour of the order parameter along the coexistence line and the critical isotherm is characterized by the critical exponents $\beta$ and $\delta$ respectively. To explain the magnetization phenomena we have to reconsider the dipole-dipole interactions, described by Weiss [14], that were deemed too weak to explain the interactions among nearest neighbours in comparison to exchange interactions. In a material that consists of an enormous number of spins though, the long ranged dipolar interactions rearrange the spin ordering into magnetic domains. The spin magnetic moments will be coupled to the electronic charge density through SOC, therefore their orientation with respect to the crystal lattice will affect their energy. This is where magneto-crystalline anisotropy comes into play, defining the energy required to align the magnetic moments into different directions. Depending on the shape of material grains, surfaces, dimensionality or applied stresses, more anisotropies arise, that create, alter or thermodynamically shift magnetic phases.

## 2.4 Geometrical frustration

The study of collective equilibrium states as well as the critical behaviour that precedes them has lately moved its focus towards geometrically frustrated solids that possess a large number of accessible ground states. Frustration, a phenomenon that appears exclusively in solids, is the result of symmetry incompatibility of local and extended degrees of freedom [15, 16].

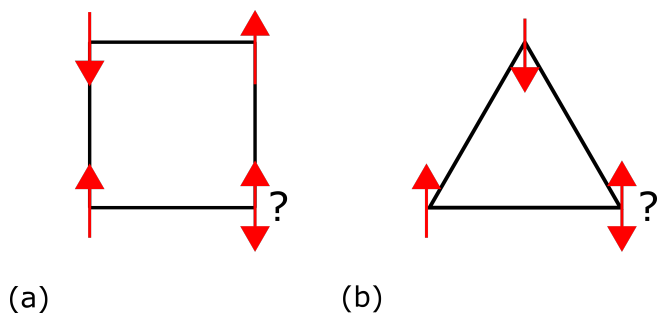


**Figure 2.3: (a):** Frustration due to impurities. A ferromagnetic bond is imposed in otherwise antiferromagnetically coupled spins. **(b):** Frustration due to topology. The antiferromagnetic exchange interaction is incompatible with the lattice geometry. These illustrations were reproduced from [17].

Considering magnetic materials, geometrical frustration arises when all pairwise interactions in the system cannot be satisfied simultaneously. Spin glasses are typical frustrated systems where random interactions between neighbouring spins create a

large number of nearly degenerate ground states. Examples of frustration that produce a spin glass are illustrated in Figure 2.3. In the first case (Fig. 2.3a) we see a square of Ising spins, antiferromagnetically coupled. The energy of the bonds can be minimized in this geometry, however, if a ferromagnetic impurity bond is introduced, one of the spins cannot satisfy the constraints of the system. In a triangle of antiferromagnetically coupled spins (Fig. 2.3b), the geometry alone imposes a frustration to one of the spins. In general, the symmetry incompatibility and an underconstraint in the spin lattice structure, give rise to degeneracies that lead to new energy minima, not predictable by the mean field theory. As a result, the strongly interacting many body system has the capacity to display new physical properties. Aside from frustrated magnetism, the structural frustration is based on which normal modes of the phonon spectrum will soften, affecting molecular bonds. Depending on the crystalline phase and ion size, certain bonds can be tilted or rotational degrees of freedom of molecules will be restricted. Depending on the electronic configuration and the strength of SOC, the Jahn-Teller distortion will be triggered or suppressed in molecules or ions of transition metal complexes [18]. However, structural disorder without frustration does not lead to new ground states, but rather in a reduction of ordering temperatures.

# Chapter 3

# Perovskites

Perovskite materials are named after the mineralogist Lev Perovski and share a similar crystal structure with the mineral $CaTiO_3$, discovered in the Ural mountains in 1839. Their flexible composition can accommodate most elements of the periodic table, organic or inorganic molecules. The magnetic and electric properties of perovskites will vary largely depending on their chemistry and structural transformations, making them very attractive functional materials in spintronic and optoelectronic applications. This chapter is an introduction to the structural and physical properties of two families of perovskite materials concerning our studies: double perovskite oxides and hybrid organic-inorganic perovskite halides.

## 3.1 Double Perovskite Oxides

Transition metal oxides have lately been drawing much interest from the solid state physics research community, owing to a rich variety of spin-orbit entangled states, which depend on their *d*-orbital electronic configuration, exchange interactions and lattice geometry [19, 20, 21]. We are particularly interested in perovskite oxides, a family of perovskite materials with structures based on calcium titanate ($CaTiO_3$) and versatile composition with high tolerance to substitutions in their cationic sites [23, 24]. Beginning from the discovery of ferroelectricity in $BaTiO_3$ [25], perovskite oxides became a topic of intense research leading to a plethora of compositions and a diversity of electronic, ionic or magnetic properties which are favourable in many applications [25, 26].

The general perovskite unit formula has the stoichiometry $ABX_3$, where A and B are cations of different sizes that bond to an X anion, usually oxides or halogens. Their crystal structure is ideally cubic, with the larger, 12-fold coordinated, A cations placed at the center and the smaller, 6-fold coordinated, B cations at the corner positions (Figure. 3.1a). This structure can be visualized as a network of adjoining $BX_6$ octahedra, often tilted or twisted, as a result of cation substitution, displacements or Jahn-Teller distortion. The degree of octahedral distortion not only affects the crystal structure, but also influences the electrical and magnetic properties of the system [27].

Octahedral distortions allow the formation of complex perovskite superstructures by adopting cations of different sizes and oxidation states at the A and B sites. The structure has the flexibility to accomodate almost all the rare earth, lanthanide

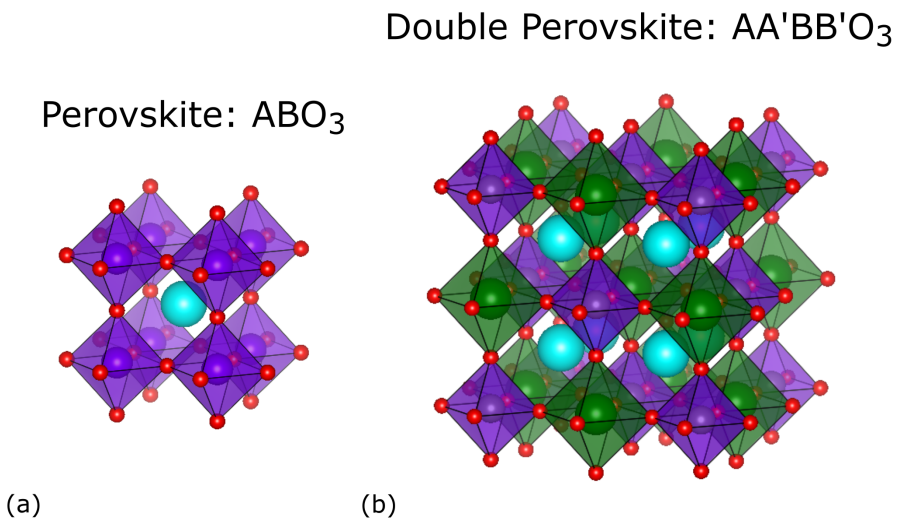


**Figure 3.1:** The perovskite oxide crystal structure of edge-sharing octahedra. **(a)**: Crystal structure of a single $ABO_3$ perovskite oxide and **(b)**: An $AA'BB'O_6$ double perovskite with a rock-salt type sub-lattice arrangement where different elements can be selected as the A,A′ and B,B′ cations. The crystal structures were generated with the Vesta software [22].

and transition metal elements. The new structure (Figure. 3.1b), termed double perovskite, has the stoichiometry $AA'BB'O_6$ and a staggered ordering of $B'O_6$ and $BO_6$ octahedra. The perovskite crystal structure and octahedral tilting based on the cation positions has been studied and classified by Glazer et al., which led to 15 different space groups [28]. Double perovskites, where A/A′ is either an alkaline, rare earth or lanthanide and B/B′ are 3d, 4d or 5d transition metals, exhibit diverse magnetic and electrical properties, including superconductivity [29], colossal magnetoresistance [30], ferroelectricity [31] and piezoelectricity [32]. The B-sites are arranged in sub-lattices depending on the B/B′ cations charge difference. Three typical sub-lattice arrangements are observed, rock-salt, layered and random [33]. The type and arrangement of B/B′ play a decisive role on the perovskite's physical properties, also displayed in our experimental results. An interplay between structure, charge and spin ordering [34, 35, 36] can generate multiple phases among magnetic, diamagnetic, metallic or insulating behaviour.

In this study we focused on Ni-Re based double perovskite compounds. Due to the interactions between the B/B′ localized $3d$ and delocalized $5d$ electrons and a strong spin-orbit coupling, these materials have been shown to present metallic to insulating behaviour, high magnetic transition temperatures and complex magnetic phases, hard magnetic character and charge carrier spin polarization [37, 38]. By joining the research on Re-based double perovskites with $LaSr_{1-x}Ca_xNiReO_6$ for $x = 0, 1$, we aim to further our understanding on how the B/B′ electronic structures, superexchange coupling and lattice geometry determine the magnetic behaviour of these compounds.

## 3.2 Organometallic Perovskite Halides

Hybrid perovskites, including methylammonium (MA) lead halides, are another unique form of $ABX_3$ perovskites consisting of organic A-site cations ($A=(CH_3NH_3)^+$), B-site cations ($B=Pb^{2+}$) and X-site halide anions ($X=Br^-$, $Cl^-$). This perovskite family has recently become one of the most attractive topics in materials research with application in photovoltaics. The current achieved power conversion efficiencies of perovskite solar cells are 25.7% for single-cell configuration and 29.8% for perovskite/Si tandem configuration [39]. One of the most critical properties of hybrid perovskites, responsible for such high efficiencies, is their long carrier lifetime. Various mechanisms have been proposed to facilitate longer lifetimes [40], however their origin remains unclear and is a matter of discussion in our experimental results. The semiconductor's energy gap can be tuned with halide doping and substitution leading to an adjustable light absorption range [41]. Owing to these semiconducting properties and a simple cell architecture [42] hybrid perovskites are considered as very promising next-generation solar cell materials.

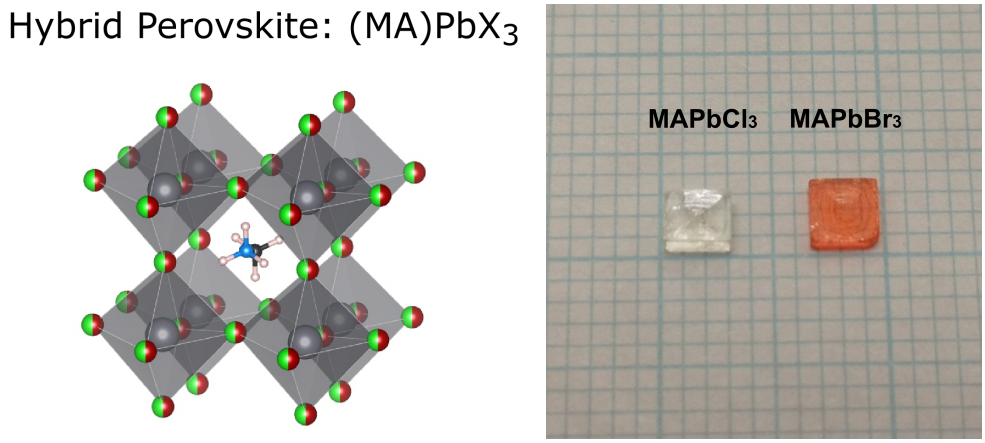


**(a)** **(b)**

**Figure 3.2: (a):** The crystal structure of a methylammonium hybrid perovskite consisting of an organic MA cation in the cubic centre, B-site cations in the octahedral centre and X-site anions on the edges of the octahedra. The Vesta software was used to produce the crystal structure. **(b):** The $MAPbCl_3$ and $MAPbBr_3$ single crystals.

The word "hybrid" indicates that the crystal is made by a combination of organic and inorganic components [43]. In a hybrid perovskite crystal, the organic cation is confined in a cage structure formed by $BX_6$ octahedra that are inteconnected via all corners to form a three-dimensional perovskite network (Figure 3.2a). The $BX_6$ octahedra show large distortion depending on the crystalline phase and size of the ions while the organic cations can reorient rapidly with reported relaxation times between 0.1-28ps [44]. The semiconducting behaviour of a hybrid perovskite arises from the inorganic $BX_3$ component, and all the critical phenomena of light absorption, carrier generation and carrier transport occur within the inorganic framework

[45]. The organic cation plays an important role in establishing the fundamental stability of the crystal and potentially provides the charge carriers with electrostatic screening [46].

The halide anion diffusion and organic molecule fluctuations have miscellaneous, favourable or unfavourable, effects to the photovoltaic function of the perovskites. A frequency dependence of permittivity may negatively affect the efficiency of solar cell [47], while a low carrier recombination rate will increase the carrier lifetime and therefore the efficiency [48]. The current density to voltage hysteresis and the lack of crystal stability are critical for the cell operation [49]. In our study of $MAPbX_3$ for X=Br,Cl we aim to identify and follow the kinetics of these ionic species as affected by temperature and illumination, with a view to fine-tune the hybrid perovskite photovoltaic performance.

In conclusion, perovskite materials present a multitude of magnetic or electrical properties and as a result have been proposed for various applications in spintronic and optoelectronic devices. However, the complexity in controlling and fine-tuning these properties, along with efforts to assure their structural integrity, naturally makes them a very wide and challenging subject of research.

# Chapter 4

# Muon spectroscopy ($\mu^+$SR)

The chapter focuses on muon spin spectroscopy ($\mu^+$SR) which was our principal experimental method. Supplementary characterization was carried out with magnetometry, electrical transport measurements, wide angle x-ray scattering (WAXS) and Raman spectroscopy.

Muon spin rotation, relaxation or resonance, abbreviatated as $\mu$SR, is a local probe technique utilizing a beam of positive or negative spin polarized muons. The muons, in their short lifetime, are implanted in our material sample. Positive muons ($\mu^+$SR) are attracted by the electron cloud and stop at interstitial sites between ions or on organic molecules. Negative muons ($\mu^-$SR) are bonding closely to the nuclei. In the present studies, we used the $\mu^+$SR module, where the spin of the implanted muons interacts with the local magnetic field distribution of its environment. This interactions yield information about the static and dynamic magnetic nature of our samples, as well as the kinematics of ions that perturb it.

## 4.1 The life of a muon

Muons in their natural environment can be found in earth's atmosphere, as products of cosmic rays collisions with atomic nuclei. A muon is an elementary, subatomic particle of the lepton family with no internal quark structure. A product of decay, the muon has a lifetime of 2.197 $\mu_s$ before itself decays into stable leptons. Although heavier than an electron, muons have a large magnetic moment (Table 4.1) making them a promising probe of magnetic environments and fields as low as $10^{-5}$ T. The muon's physical properties together with the undestanding of our ability to extract the probing information gave birth to $\mu$SR.

| charge | spin | magn.moment | $\gamma/2\pi$ | lifetime | mass |
|---|---|---|---|---|---|
| $+e$ | 1/2 | $3.18\mu_p$ | $13.5kHzG^{-1}$ | $2.197\mu s$ | $206.768m_e$ $= 0.1124m_p$ $= 105.7MeV$ |

**Table 4.1:** Positive muon properties.

Muons naturally arrive on earth with a flux of approximately 1 $muon/m \cdot cm^2$ and

are highly energetic ($GeV - TeV$). However, these values are far from suitable for experimental purposes. For a muon to be used as a probe, higher fluxes around $10^4 - 10^5 \mu/s \cdot cm^2$ and lower energies of $10 - 100\ MeV$ are required [16]. Such intense beams of muons can be provided in hadron particle accelerator facilities, the power sources of a $\mu$SR experiment.

The process of creating positive muons is a sequence of collision and decay. Initially, a high energy proton beam is prepared and directed onto a graphite or beryllium target. These collisions result in the creation of positive, spinless pions

$$p + p \rightarrow \pi^+ + p + n \tag{4.1}$$

,which have a lifetime of 26.033 $ns$ and eventually decay into positive muons.

$$\pi^+ \rightarrow \mu^+ + \nu_\mu \tag{4.2}$$

We are interested in pions that lie at rest in the target, in the laboratory frame. Consequently, the created muon and muon neutrino must have opposite linear momenta. The pion also has zero spin so the muon and neutrino spins must cancel out. The fact that the muon neutrino has a negative helicity, from a spin aligned antiparallel to its orbital angular momentum, dictates that the positive muon must be aligned likewise. Therefore, by selecting pions at rest in the target, it allows us to produce an almost perfectly spin polarized beam of muons with energies higher than 4 MeV, which can then be directed towards our sample. When the spin polarized muons penetrate the sample, first they take part in a series of rapid Coulombic effects. They lose their energy, down to a few keV within $0.1 - 1\ ns$, by scattering with electrons and ionizing atoms. Electron capture and loss results either to a muonium ($\mu^+ e^-$) atom that is lost in inelastic collisions with neighbouring atoms, or reduces the muon energy to a few eV. In the second part of their path, muons do not disturb the system and are well away from the vacancies that may have been created behind them. Eventually muons thermalize in the material, with their spin polarization still intact. In the most impactful moments of their lives, muons interact with the local magnetic environment of the material and finally decay after a lifespan of $\tau_\mu = 2.2\ \mu s$. This decay creates a positron, an electron neutrino and a muon antineutrino that carry information of the former interaction in their momenta.

$$\mu^+ \rightarrow e^+ + \nu_e + \bar{\nu}_\mu \tag{4.3}$$

Just before decaying, the muon rests at an interstitial site, meaning that from conservation of linear momentum the momenta of the emitted positron and neutrinos must sum up to zero. The electron neutrino and muon antineutrino have a total of zero angular momentum, therefore the balance of angular momenta depends on the positron. The options a positron has are either a positive helicity, where the spin and orbital momenta are parallel, or a negative helicity with antiparallel momenta. However, conservation of the total angular momentum together with parity violation introduced from the weak interaction involved in the decay [50] result to a higher probability for the positron to be emitted in the direction of the muon spin.

This leads to an asymmetric emission of positrons, known as the forward-backward asymmetry [51]. The angular distribution of probability for the emitted positrons with respect to the muon spin direction is described as:

$$N(\theta) \propto 1 + A(E)\cos\theta \tag{4.4}$$

The asymmetry parameter $A(E)$ depends on the positron kinetic energy [52]. As a result, the shape of the distribution changes Figure 4.1a from, e.g, a cardioid for the maximum energy to an averaged distribution (blue disk) for an integration over all positron kinetic energies, which gives $A_{avg}(E) = 0.33$.

## 4.2 The muon as magnetic probe

Position sensitive detectors are placed around the sample, which can systematically detect emitted positrons with picosecond timing and reconstruct their flight path. By counting millions of positrons, which are emitted asymmetrically towards different detectors, we can construct a polarization function of the muon spin ensemble under the effect of local fields.

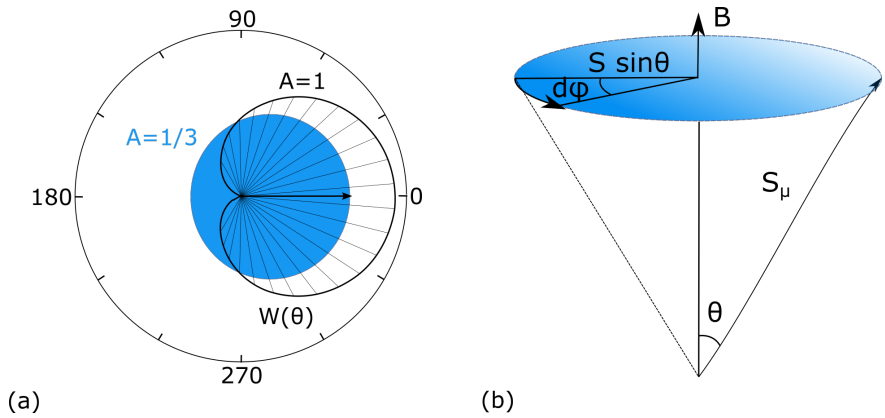


**Figure 4.1: (a)**: Two angular distributions $N(\theta)$ of the positron emission direction relative to the muon spin (bold arrow). The cardioid corresponds to the most energetically emitted positrons while the blue disk represents an average over all positron kinetic energies. **(b)**: Larmor precession of a muon's spin around a magnetic field. Reconstructed from [51].

The number of positron events at time $t$ on the forward and backward detector, with respect to the initial spin direction, is related to the number of decaying muons. In zero field or applied field parallel to the muon spin, for the full solid angle, the time evolution of the positron counts is described by an exponential decay:

$$N_{F|B}(t) = N_0 e^{-t/\tau_\mu}\left[1 \pm \alpha \frac{P_\mu(t)}{P_{max}}\right] \tag{4.5}$$

,where $N_0$ is a normalization constant, $\tau_\mu$ the muon mean lifetime, $\alpha$ the initial asymmetry for the spectrometer which is empirically determined, $P_\mu$ the muon polarization function, and $P_{max}(\approx 0.25)$ the maximum asymmetry [53]. The normalized polarization function can then be calculated from the counts of the forward and backward detectors:

$$\alpha \frac{P_\mu(t)}{P_{max}} = \frac{N_B(t) - N_F(t)}{N_B(t) + N_F(t)} \tag{4.6}$$

If a field is applied perpendicular to the muon spin or, in case of a magnet, an intrinsic magnetic field with perpendicular components emerges, then the muon magnetic moment will precess around it as a result of a torque:

$$\vec{\tau} = \frac{d\vec{S}}{dt} = \gamma \vec{S} \times \vec{B}_{local} \tag{4.7}$$

known as Larmor precession (Figure 4.1b). The frequency of the muon spin precession $\omega = d\varphi/dt = \gamma_\mu B_{local}$, where $\gamma_\mu$ the gyromagnetic ratio of the muon (Table 4.1), is experimentally observed and gives a measure of the local field. For a uniform field at all muon sites the polarization function is described as:

$$\alpha P_{\mu,norm}(t) = \cos^2\theta + \sin^2\theta \cos(\omega_\mu t) \tag{4.8}$$

In general, the polarization function will depend on a distribution of fields in different regions of the material, and also the fluctuations of these local fields with time [54, 55]. If the directions of the local magnetic fields are entirely random, then a spatial average over all directions will give:

$$\alpha P_{\mu,norm}(t) = \frac{1}{3} + \frac{2}{3}\cos(\omega_\mu t) \tag{4.9}$$

The oscillating part (Fig. 4.2a) describes the sample's magnetic order [56, 57]. As we increase the sample's temperature this oscillation will decrease until it vanishes above the Curie temperature. Equation (4.9) is used to describe polycrystalline magnetic samples, since crystallites have no preferred orientation [52]. By taking advantage of the spin polarization and sampling of different regions in the material, we can identify ferromagnetism or antiferromagnetism and measure the volumic fraction of these magnetic transitions. Muons may rest at more than one equivalent sites and the field distribution at each muon site is an interplay of individual magnetic fields (applied, dipolar, demagnetization, hyperfine field). If the magnet is not perfectly ordered, then the local field will take a wide range of values and the oscillations will be damped. Since the muons interact with a local magnetic field distribution rather than a particular field, the local field contribution can be described by a gaussian (or a lorentzian) distribution with width $\Delta/\gamma_\mu$ around zero. Consequently equation (4.9) averages to:

$$\alpha P_{\mu,norm}(t) = \frac{1}{3} + \frac{2}{3}(1 - \Delta^2 t^2)e^{(-\Delta^2 t^2/2)} \tag{4.10}$$

which is known as the Kubo-Toyabe (KT) function [58]. Falling from unity, a minimum is located at $t = \sqrt{3}/\Delta$ and depending on $\Delta$ the function obtains an average value 1/3 (Fig. 4.2b). This polarization function describes the experimental data when the contributing local fields are random and the average field at the muon site is zero [51, 58]. In general the depolarization depends on static distribution of local fields, as well as fluctuation of fields in time, and can be described by a variety of functions, each one weighted with an asymmetry parameter:

$$\alpha P_{\mu,norm}(t) = A_1 f_1(t) + A_2 f_2(t) + ... + A_n f_n(t) \tag{4.11}$$

,in order to describe the relaxation and possible oscillations of the muon spins with time.

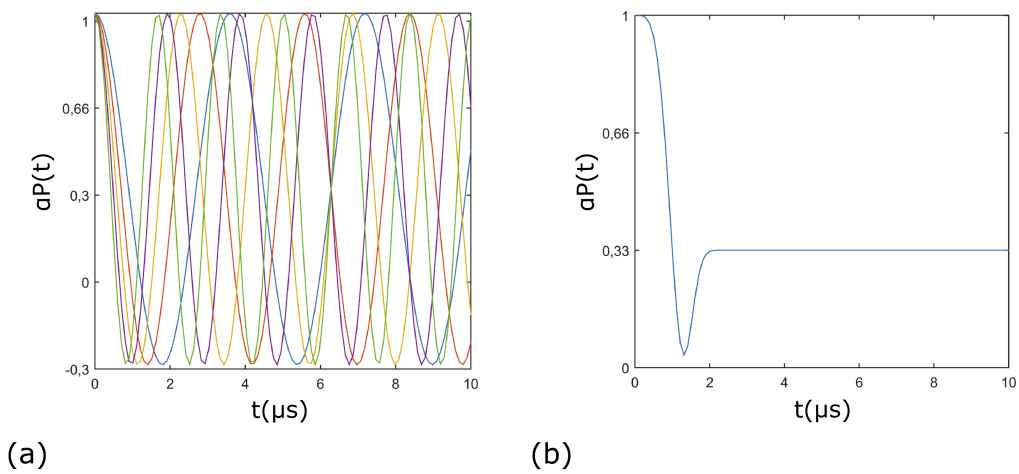


**Figure 4.2:** **(a)**: Time evolution of the polarization function (Eq. 4.9). Each colour represents a different magnetic field amplitude. **(b)**: Time evolution of the field averaged Kubo-Toyabe polarization function (Eq. 4.10). Reconstructed from [59].

The muon spin interacts with both electronic and nuclear magnetic moments. When a magnetic order is not present, the electronic moments are fluctuating too quickly for the muon spin to sense them. The muons will depolarize only by static and randomly oriented nuclear dipole moments and may also be described by a Kubo-Toyabe type function. The interaction between the muon spin $S$ and the nearby nuclear spins $I$ is described by the hamiltonian

$$H = \sum_{j=1}^{N} \left( H_j^d + H_{\mu j}^q + H_{\kappa j}^q \right) \tag{4.12}$$

,where $H_j^d$ is the dipole-dipole interaction between the positive muon and the $j_{th}$ nucleus, $H_{\mu j}^q$ represents the quadrupolar energy of the nuclear spin $I_j$ due to the electric field gradient generated by the muon, and $H_{\kappa j}^q$ represents the quadrupolar energy of the nuclear spin due to the electric field gradient of the crystal. The arrangement and migration of ions in the lattice will alter the distribution of nuclear fields. When

an ion starts to diffuse, the relaxation rate is suppressed due to motional narrowing. The creation and diffusion of muoniums is another possible process that will affect the relaxation rate. This scenario can be identified from a missing asymmetry when the muons are forced to precess to an external field. The polarization function gives us the field fluctuation rate, which is directly proportional to the ion diffusion rate coefficient [60, 61]. Therefore, ionic diffusion and their activation energies can be identified, while the signals from magnetic and non-magnetic ions are distinguishable with $\mu SR$.

Muons are distributed in groups of equivalent lattice sites, therefore each component of the muon spin relaxation represents a volumic fraction of the material's response. This enables us to study partly ordered systems and the evolution of their magnetic phases in a material [62, 63, 64]. In addition, phonon activated muon and atom hopping, impurities and defects also contribute to field fluctuations [51, 52]. Consequently, the local environment of the muon together with the sample's intrinsic magnetic properties determine the spin relaxation of the muon ensemble.

## 4.3 The $\mu^+$SR experiment

A $\mu SR$ experiment takes place at a large scale facility, where a cyclotron or a synchrotron are used to provide a continuous or pulsed source of muons. Two types of muons can be provided, surface or decay muons. Surface muons are emitted from the decay of positive pions which lie at rest on a target, as described in the previous section. These muons have low energy ($\sim$4 MeV), a narrow energy distribution, and they are 100% spin polarized. Decay muons originate from pions decaying while in flight, they have higher energies and are used in measurements where high penetration depths are required, a typical case is in pressure cell experiments. In our studies we used positive, spin polarized, surface muons.

Time differential or time integral measurements can be performed with both continuous and pulsed sources. During a time integral measurement there is a continuous flow of muons into the sample, while for a time differential measurement only one muon or muon pulse is allowed to hit the sample at a time [53]. Here we consider only time differential measurements since this is the framework of our studies and the most common approach.

A continuous source, such as the PSI [65] and TRIUMF [66] beamlines used in papers I and II, offer a high time resolution that allows us to measure precession frequencies up to 5 GHz. A continuous source generates high fluxes of muons ($10^8 m/A \cdot s$), yet the data rate is low due to the time differential scheme. Alternatively, a pulsed source, such as the ISIS beamline [67, 68] used in paper III, offers high measuring rates, however, the time resolution is limited ($\sim$10 MHz) depending on the pulse width. Pulsed sources are more versatile since they can combine time integral and differential measurements, and they are compatible with pulsed laser, RF field, pulsed magnetic field excitations, etc.

The purpose of a $\mu SR$ measurement is to record the time evolution of the muon polarization from an ensemble of muons implanted into a material. Here we take a continuous source as an example, still the same procedure is followed for a pulsed source. In a time-differential $\mu^+SR$ measurement, we begin with a spin polarized,

positive muon flying down the beamline, with spin $s_\mu$ antiparallel to its momentum $p_\mu$, and through a muon detector that sets the starting time of the measurement (Fig. 4.3). The muon continues to hit and penetrate our sample until it rests at an interstitial site. There the muon spin interacts with local, intrinsic and applied, fields until it decays. The generated positron is emitted with high probability along the direction of the spin at the decay. One of the detectors surrounding the sample collects the emitted positron and determines its momentum. The detection of the positron sets the stopping time of that single measurement and the same process is repeated until sufficient statistics are achieved. From the distribution of positron momenta around the sample we create an asymmetry spectrum that represents the evolution of the muon polarization (Fig. 4.4). Three types of measurements are possible [69, 70], depending on whether an external magnetic field is applied or not, namely zero field (ZF), transverse field (TF) and longitudinal field (LF), with respect to the muon spin.

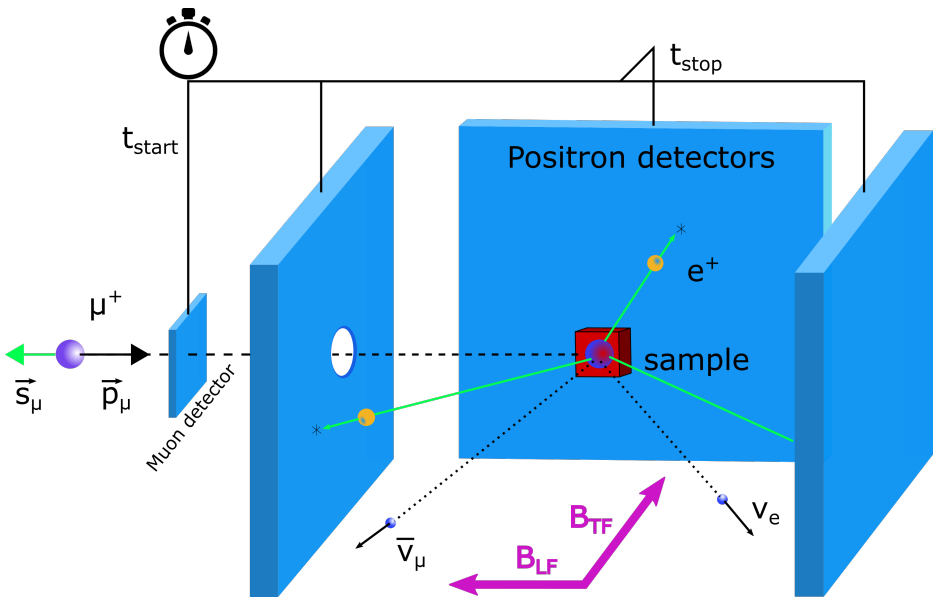


**Figure 4.3:** Representation of a time differential $\mu^+SR$ measurement. An incoming spin polarized muon is first detected by the muon detector which sets the starting time of a measurement. The muon then flies through the windows of the positron detectors and the cryostat, and is implanted into the sample. In the interstitial sites of the lattice the muon spin will interact with the surrounding magnetic fields. These fields may be intrinsic or applied perpendicular ($\mathbf{B}_{TF}$) or parallel ($\mathbf{B}_{LF}$) to the muon spin. The muon eventually decays to a positron, an electron neutrino and a muon antineutrino. The positron momentum is most probable to be parallel to the muon spin at the moment of decay. One of the positron detectors will collect the emitted positron, determine its flight path and set the stopping time of the measurement. This schematic was inspired from [71].

For the LF and ZF experiments, a magnetic field $B_{LF}$ is applied parallel to the initial muon spin polarization direction, or no field is applied respectively (Fig. 4.3). The asymmetry spectra is constructed from signals of the detectors placed in the forward and backward direction (Fig. 4.4a) with respect to the muon spin $s_\mu$.

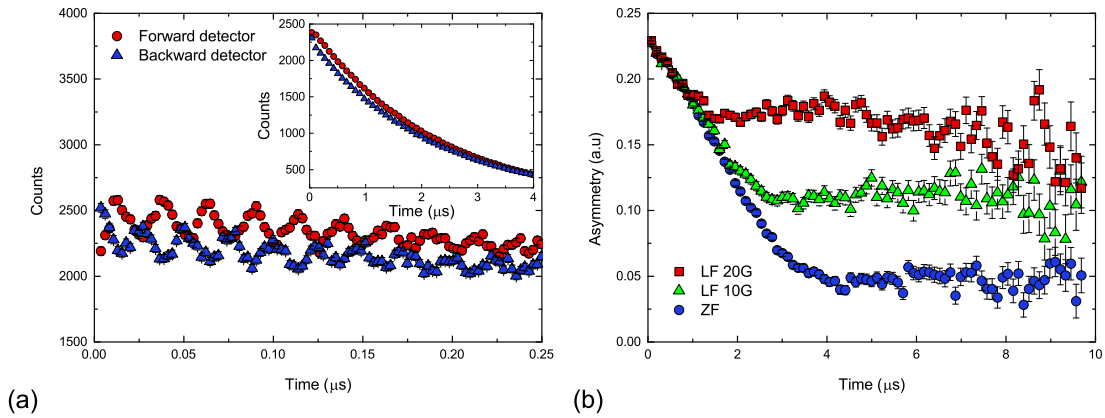


**Figure 4.4: (a)**: Positron counts as a function of time, in the short time domain, for the forward and backward detector. The presented data are ZF measurements at 2K. Oscillations are observed, therefore a magnetic order exists. The inset shows the same data in the long time domain. **(b)**: The decoupling of muon spins from static internal fields with the application of longitudinal fields. With a high enough longitudinal field the spin polarization will be time independent.

In ZF measurements, for a random orientation of internal fields, the asymmetry will decrease with time until it reaches an average value (Eq. 4.10). If a magnetic ordering is present, the muon spins will precess with the intrinsic magnetic field (Fig. 4.4a). The asymmetry of the forward and backward detector positron counts is then described by an oscillatory polarization function (Eq. 4.9). From the components of polarization functions used to describe the asymmetry spectra we can identify the type of magnetic ordering and spin dynamics, each represented as volumic fraction of the sampled material.

During an LF measurement (Fig. 4.4b) the applied field is parallel to the muon spin, which is then forced to relax about its original direction. As the applied field is increased, the muon spin becomes even more pinned and the exponential relaxation seen in Figure 4.2b is lifted towards unity. With a longitudinal field (up to several T) we can extract measures of the magnetic field distribution, dynamics, diffusion of magnetic ions or formed muoniums. An LF measurement is typically used to distinguish the static from the fluctuating field distributions of nuclear and electronic nature, as the application of a longitudinal field will decouple the muon spin from the effect of static internal fields.

In the TF configuration, a magnetic field $B_{TF}$ (up to ∼10 T) is applied perpendicular to the muon spin. Signals from the detectors with their normal perpendicular to the applied field are used to construct the asymmetry spectra (Fig. 4.3). The applied field will cause the muon to precess with a frequency $f_\mu = \gamma_\mu B_\mu / 2\pi$ , proportional to the local field at the muon site. In case of an intrinsic, inhomogeneous field distribution, the oscillations will dephase. Below a magnetic transition the oscillations will be progressively damped. The evolution of the asymmetry component of this polarization function with temperature will give us an approximation of the magnetic transition temperature.

# Chapter 5

# Results and Discussion

This chapter summarizes the main results of the appended papers I-III. The systems studied belong to the perovskite family of materials. In papers I and II we focus on the emerging magnetic phases of transition metal double perovskite oxides, as a consequence of cation interaction and cation substitution. In paper III we investigate the ion kinetics in hybrid organic-inorganic perovskite halides through structural transitions, as affected by anion substitution, temperature and illumination. The entirety of this section is dedicated to $\mu^+SR$ measurements in both continuous and pulsed sources, as a function of temperature and applied magnetic fields.

## 5.1 Magnetic phases of Ni-Re based double perovskites

The research presented in papers I and II aims to reveal the formation and dynamics of multiple magnetic phases in Ni-Re based double perovskite oxides. We observe how cation substitution and structural distortions determine the magnetic ordering, along with how the spin correlations evolve with temperature. For these studies we employed $\mu^+SR$ at a surface muon, continuous source with a time differential setup, as described in section 4.3. The $x = 0$ and $x = 1$ compositions of the $LaSr_{1-x}Ca_xNiReO_6$ double perovskite oxide were magnetically investigated in the temperature range of 2-300 K, under TF, ZF and LF conditions. Samples of the same polycrystalline powder batch have been previously studied by Jana *et al.* [72] and were found to be insulating magnets. X-ray powder diffraction results have shown no impurities in the samples, while both x-ray and neutron diffraction data were fitted under the $P2_1/n$ space group at all measured temperatures [72]. Nevertheless, bulk magnetometry and neutron diffraction results created ambiguities as to the magnetic structure of both compounds. Therefore, we took on the challenge to investigate the magnetic ordering in these materials. To cover a wide frequency range in magnetic dynamics and verify our results we performed both bulk magnetometry and $\mu^+SR$ measurements. These measurements exposed a series of magnetic phases, above and below the respective critical temperatures, that strongly depend on the exchange of cations on the A′ site of the double perovskite introduced in section 3.1.

Both compounds present magnetic ordering as a result of the interacting $Ni^{2+}$ and $Re^{5+}$ magnetic sublattices. In section 2.2 we have highlighted the exchange interactions that sufficiently predict ferro- or antiferromagnetism. The principle ex-

change interaction in this system is a superexchange interaction between the Ni and Re cations. Superexchange depends on orbital overlap and therefore, on the Ni-O-Re bond angle. Previous studies have highlighted the effects of cation substitution in the magnetic properties of double perovskites through exchange interactions and spin-lattice coupling [73, 74, 75, 76]. A substitution of the $Sr^{2+}$, A′ site cation with the smaller $Ca^{2+}$ is likely to distort the octahedra and affect this B-O-B′ bond angle. In the $x = 0$ crystal a ∼180° angle is expected, which promotes ferromagnetic interaction, while for $x = 1$ the angle is narrowed and antiferromagnetic interaction is more favourable. Furthermore, the interplay between first and higher order neighbour interactions can effectively alter the type of magnetic ordering [77]. The strong SOC of the 5d transition metal Re creates a coupling between the spin structure and the crystal symmetry through the orbital momenta (section 2.1). This coupling is the source of Jahn-Teller distortion of the octahedra and a magnetocrystaline anisotropy, indications of which are the high remanence and coercivity values observed in both compounds.

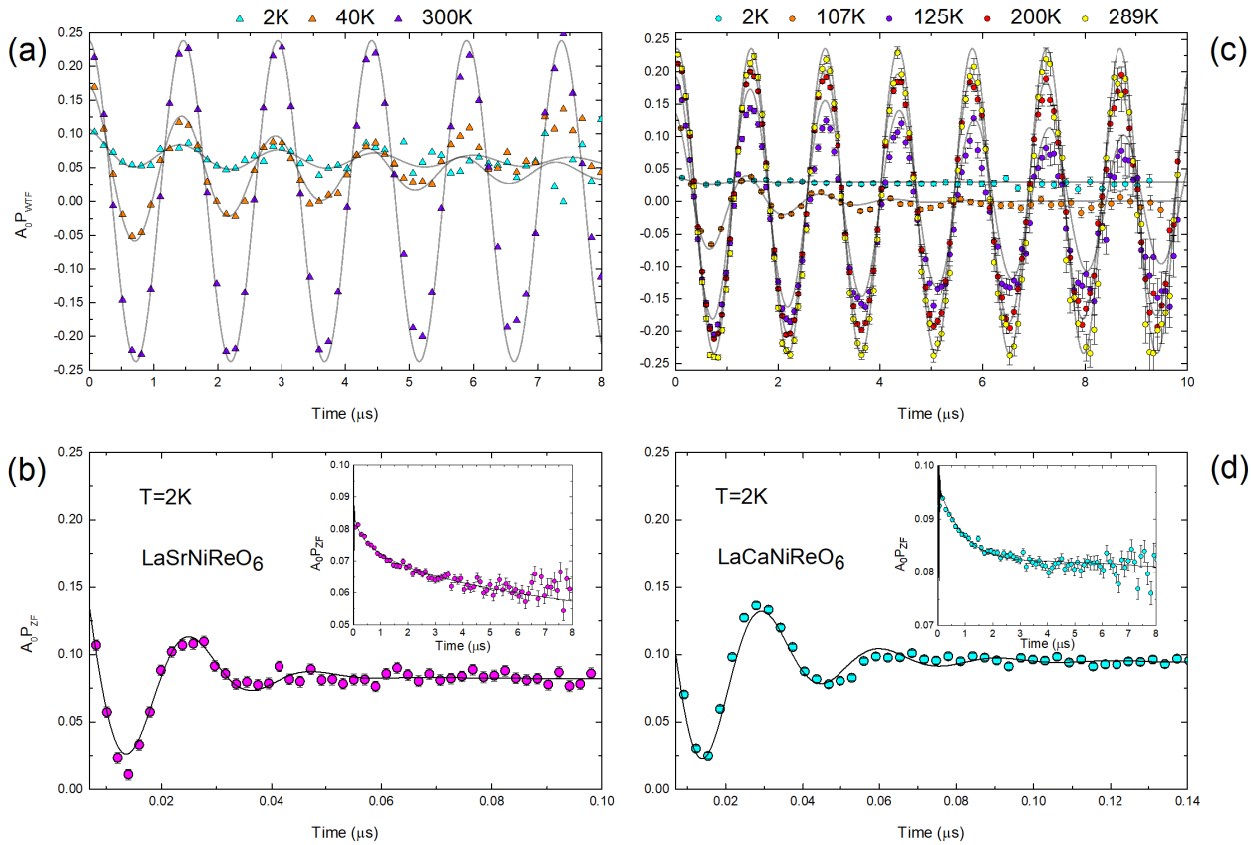


**Figure 5.1: (a,b)**: transverse (TF) and zero (ZF) field time spectra of $LaSrNiReO_6$. **(c,d)**: TF and ZF time spectra of $LaCaNiReO_6$. The insets show the same data in the long time domain [78, 79].

Papers I and II focus on the $x = 0$ and $x = 1$ case respectively. In the following, the $x = 0$ compound will be referred as "Sr" and the $x = 1$ compound as "Ca" for clarity. From TF $\mu^+SR$ measurements on each sample we were able to approximate a magnetic transition temperature (Fig. 5.2 a,d) from the evolution of the polariza-

tion function's asymmetry component. In both samples, the TF oscillations remain damped well above the transition temperature, as seen in Figures 5.1 a,c , an indication of persisting magnetic components. In both samples the paramagnetic state is not reached until above ∼250 K, as observed also in our DC susceptibility data.

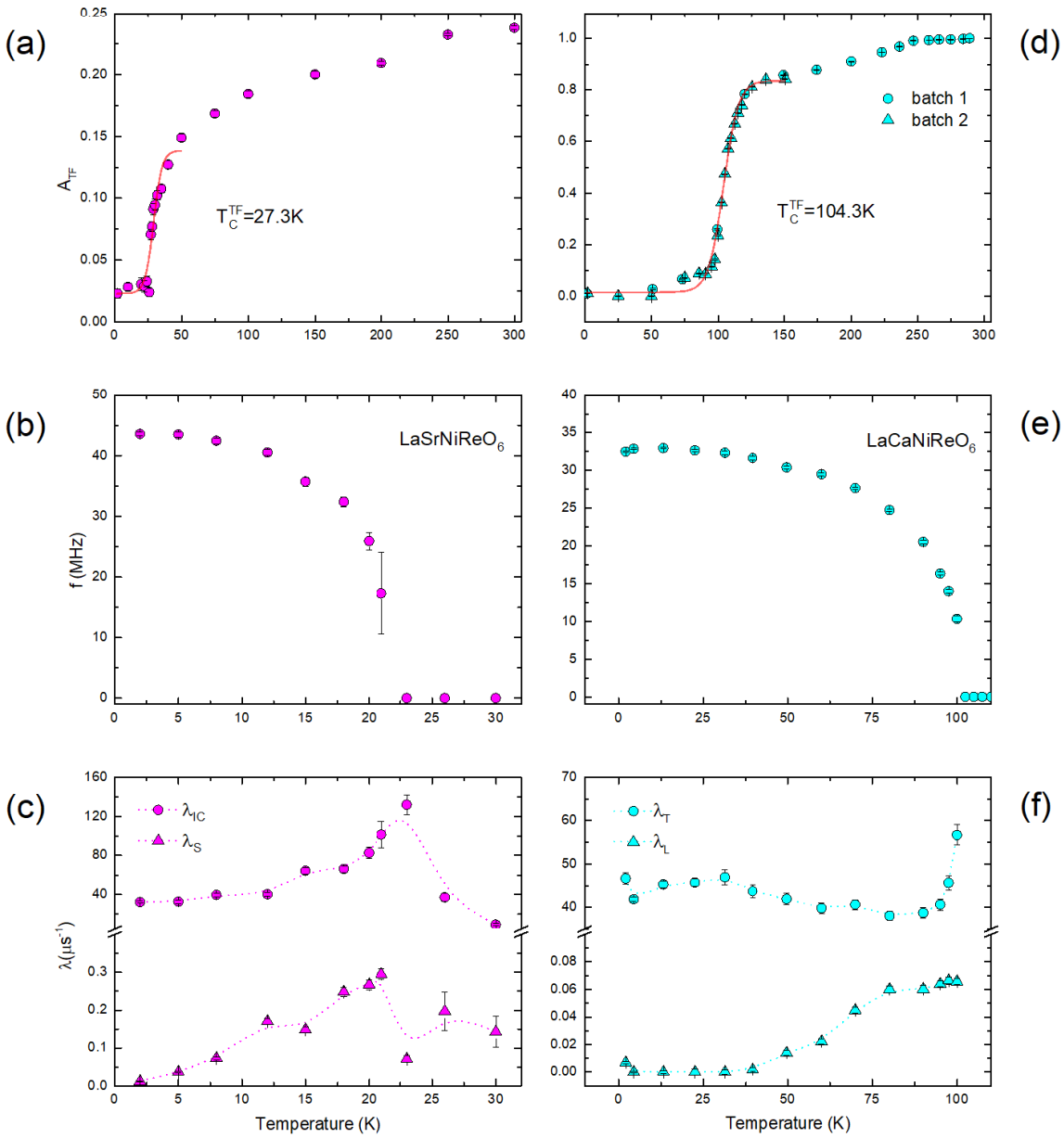


**Figure 5.2:** **(a-c)**: The TF asymmetry, ZF frequency and depolarization rate components of the polarization function for $LaSrNiReO_6$. **(d-f)**: The respective components for $LaCaNiReO_6$ [78, 79].

ZF measurements followed to directly probe the intrinsic magnetic field distributions of the two compounds. At T=2 K the muon spectra from both compounds exhibit a highly damped oscillation in the short time scale (Fig. 5.1 b,d). The spectra in this time scale were fitted with an exponentially relaxing Bessel function for the Sr compound. The use of a Bessel function denotes a magnetic ordering with

periodicity that is not commensurate with that of the crystal lattice [80]. The respective spectra for the Ca compound were fitted with an exponentially relaxing cosine function that refers to commensurate order. The transition from a commensurate to an incommensurate order reveals that the A′ site cation substitution with Sr creates a competition between ferromagnetic and antiferromagnetic interactions among the first and possibly higher order neighbours of the Ni and Re cations. Although numerical simulations predicted two possible muon sites for these systems, a single oscillation frequency shows that they must be magnetically equivalent. These frequencies are proportional to the internal magnetic field (section 4.2) and from their temperature dependence (Fig. 5.2 b,e) we are able to accurately determine the critical temperatures $T_C^{Sr}$ =23 K and $T_C^{Ca}$ =103 K. The highly damped oscillations represent magnetic systems that are not static in a long range. In Figures 5.2 c,f we show the depolarization rates originating from field components perpendicular ($\lambda_{IC}, \lambda_T$) and parallel ($\lambda_S, \lambda_L$) to the muon spin. The perpendicular components reflect the field distribution seen by precessing muon spins in the short time domain. In addition, both parallel and perpendicular components contain information about spin dynamics represented by the spectra at longer times. All rates are increased, as expected, when we approach the critical temperatures, since a phase transition is always characterized by high dynamics in the system. At lower temperatures though, the depolarization rates are still significant, meaning that the muons interact with a fluctuating magnetic environment. From the oscillatory signals, the evolution of magnetic susceptibility below transition and the description of the physical system, we expect a ferrimagnetic state as a result of the ferromagnetic/antiferromagnetic interaction between ferromagnetically aligned sublattices of uneven Ni and Re moments. The persisting depolarization rates however reveal that this state is modulated by interacting spin waves generated by the active local fields and thermal energy.

Above transition temperature the muon spectra from both materials present no oscillations but still consist of a fast and slow spin relaxing component. These temperature regions were described by a different set of field distributions for each material. However, both approaches effectively describe a similar picture. There exist regions of relatively strongly and weakly correlated spins that create a dense and dilute spin environment on a paramagnetic background. These correlations cease to exist with increasing temperature, and eventually both samples become paramagnetic above ∼250 K.

## 5.2 Ion kinetics in the hybrid methylammonium lead halide perovskites

The studies on paper III focus on the kinetics of ionic species and how these evolve with temperature and are affected by illumination. For the $\mu^+SR$ measurements presented in paper III we took advantage of the high counting rates acquired with the use of a pulsed muon source. The studied single crystals were the hybrid organic-inorganic perovskites $(CH_3NH_3)PbX_3$ for X=Br, Cl presented in section 3.2. These materials are not expected to develop any magnetic ordering, therefore a good time

resolution for fast relaxing components is not required. Hybrid organic-inorganic perovskites attracted a lot of attention due to their long carrier lifetime leading to a large carrier diffusion length and therefore a good photovoltaic performance [81, 82]. However, halide diffusion impedes their performance [83], while fluctuations of the organic cation may act in favour of the semiconducting properties [84, 85] or disrupt the crystal stability [86]. Here we aim to reveal the dynamics of the local nuclear magnetic fields, as affected by structural transitions, ion diffusion, fluctuations of the organic MA cation and illumination. To this end, TF, ZF and LF measurements were performed as a function of temperature in the 30-340 K range, while the sample was in a dark or illuminated enviroment.

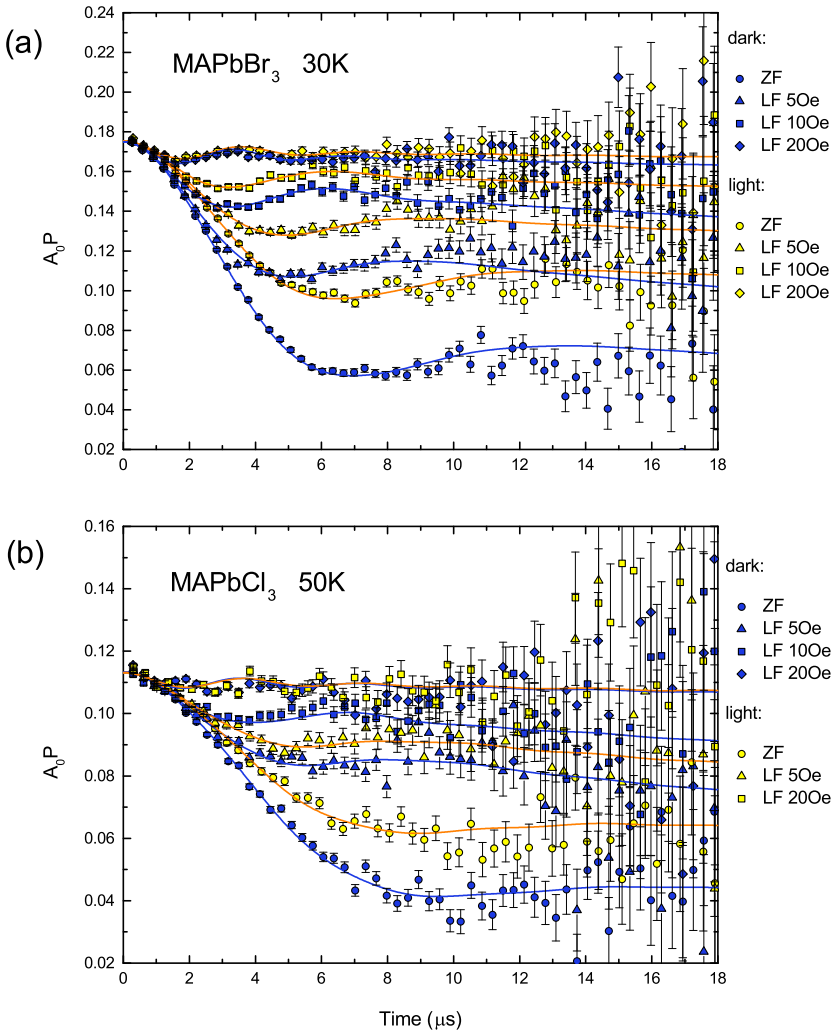


**Figure 5.3:** Zero field (ZF) and longitudinal field (LF= $5, 10, 20$ Oe) time spectra recorded at **(a):** $T$ =30 K for $MAPbBr_3$ and **(b):** $T$ =50 K for $MAPbCl_3$, in the dark and under illumination.

The ZF and LF spectra were fitted with a dynamically modified KT function (section 4.2) in order to include fluctuations of the field distribution. Examples of the fitted time spectra, at low temperatures, for both materials, are shown in Figures 5.3. The parameters of the field distributions and their fluctuations were

fitted as common on both ZF and LF experimental data. In that way, we were able to identify and follow the evolution of both static and dynamic field sources of the muon spin depolarization signal.

The $MAPbBr_3$ (Br) and $MAPbCl_3$ (Cl) crystal structures are found to be cubic at room temperature. As temperature decreases the crystals rearrange into structures with lower symmetry [87, 88]. The Br crystal transforms from cubic to tetragonal at ∼220 K and from tetragonal to orthorhombic at ∼145 K. The Cl crystal undergoes similar transitions at ∼180 K and ∼175 K. DFT calculations on the electrostatic potential were carried out for all structural phases. From the potential minima in the different crystal structures we were able to identify the possible muon sites. Then, the dipole fields were calculated at these muon sites. The MA molecule, which is enclosed by the $PbX_6$ octahedra, also contributes to the dipole field with dipoles being either static or rotating in an independent or correlated manner. Depending on whether the H, C, N nuclear moments are considered static or motionally narrowed, different field distributions were calculated.

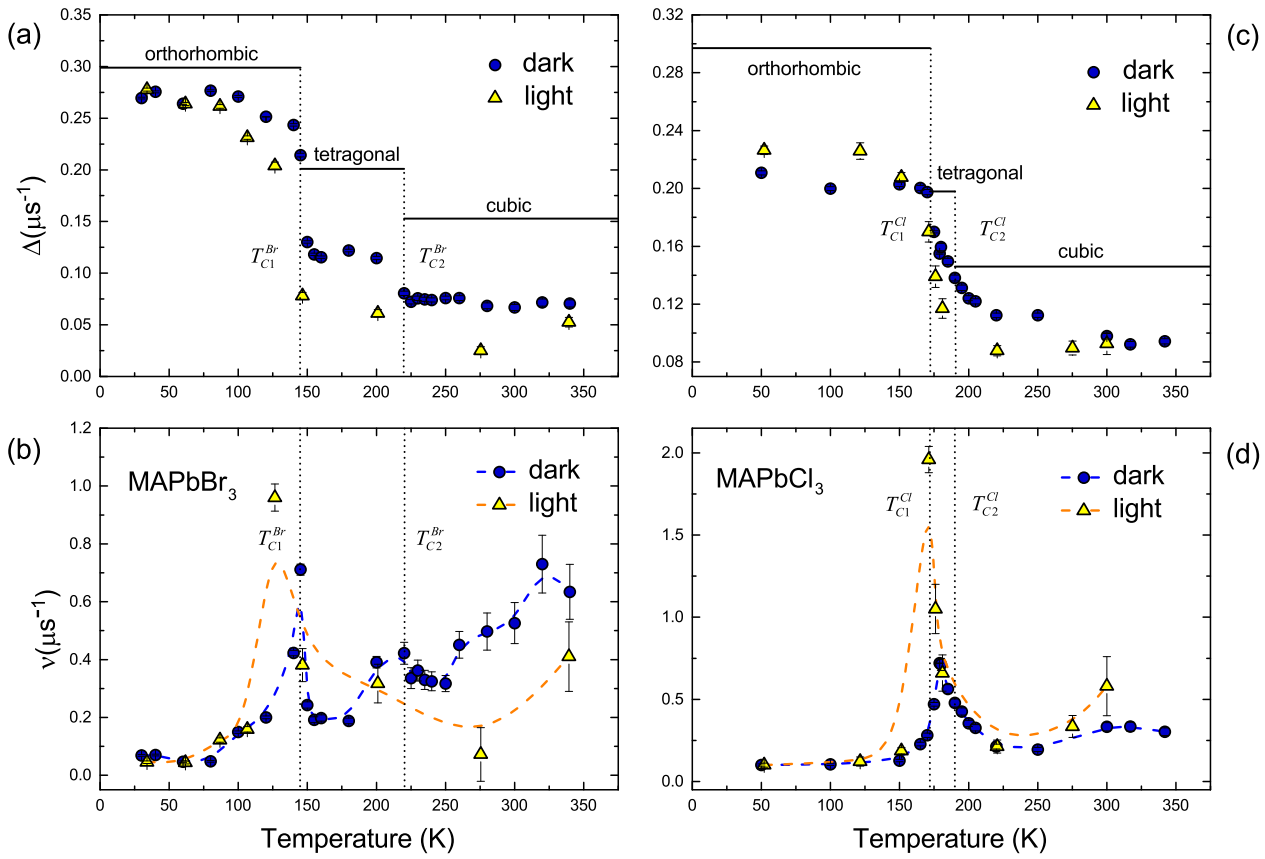


**Figure 5.4:** Temperature dependent **(a,c):** field distribution width and **(b,d):** field fluctuation rate of $MAPbBr_3$ and $MAPbCl_3$, in dark and illuminated environment.

The field distribution width, $\Delta$, and the field fluctuation rate, $\nu$, are presented as a function of temperature in Figure 5.4. For both Br and Cl crystals $\Delta$ appears to be constant and $\nu$ is small at low temperatures. The solid parallel lines (Fig. 5.4 a,c) show the calculated dipole field values formed predominantly by the H, Br and Cl nuclear spins (section 4.2). While the experimental and theoretical values agree for

the Br crystal in the orthorhombic phase, in the Cl case the deviation is attributed to a variation of the muon site. Moving up in temperature, $\nu$ increases and then drops exponentially (Fig. 5.4 b,d) around the orthorhombic-tetragonal structural transition temperature $T_{C1}$. For this new crystal symmetry the muons will experience a new field distribution in the ionic lattice and thus indirectly map the structural transition. The calculated value of a static field distribution width does not agree with the experimental value of $\Delta$. However, if we consider the narrow peaks of $\nu$ to stem from fluctuations of the organic molecule, then the calculated $\Delta$ for a motionally narrowed MA molecule are closer to the experimental values. Going higher in temperature, we consider the increase in $\nu$ to be mainly a result of $Br^-$ and $Cl^-$ diffusion. For the Br crystal at $T_{C2}$ we observe another drop to a lower $\Delta$ value, while for Cl the $\Delta$ value drops continuously and then stabilizes above $T_{C2}$. Again, the calculated values, including a motional narrowing from the MA fluctuations, produce a closer match to our observations.

The main effect of illumination is considered to be an enhancement of MA fluctuations for both crystals. The motional narrowing of $\Delta$ is increased as MA fluctuations appear with respect to each structural phase. The peak of $\nu$ around $T_{C1}$ is increased and shifted at lower temperatures, an indication that MA fluctuations determine the structural transitions. In conclusion, we discuss the effect of illumination in terms of photoinduced charge carriers interacting with the MA cations, which in turn results in an electrostatic screening providing the carriers with a long lifetime.

# Chapter 6

# Conclusions and Outlooks

This thesis is focused on the study of correlation effects in inorganic oxide and organometalic halide perovskites with muon spectroscopy. Papers I and II investigate the magnetic phases of the double perovskite polycrystals $LaSr_{1-x}Ca_xNiReO_6$ (x=0,1) and how the substitution of Sr with Ca affects the magnetic ordering. In the case of Sr a magnetic ordering with periodicity incommensurate to the periodicity of the crystal lattice is observed below $T_c$=23 K. This is an effect of an interplay between ferro- and antiferromagnetic coupling of the Ni and Re cations. When Sr is exchanged with Ca the ordering is developed at $T_c$=103 K and becomes commensurate as antiferromagnetic coupling is expected to prevail. For both compounds the magnetic order appears in the form of ferrimagnetic domains that are modulated by interacting spin waves of the Ni and Re sublattices. Above $T_c$ a fraction of the spins remains correlated until gradually the paramagnetic state of randomly oriented magnetic moments is reached above 250 K. Further ZF and LF studies with higher statistics and in a larger time window would potentially reveal more details on the static and dynamic field contributions in the $T_c$<T<250 K region.

Paper III explores the dynamics of nuclear dipole fields in the hybrid perovskite single crystals $(CH_3NH_3)PbX_3$ (X=Br,Cl) and how these are affected by structural transitions, rotational dynamics of the organic molecule and $Br^-$, $Cl^-$ diffusion. Values of the nuclear dipole field distribution width were experimentally extracted and compared with numerical calculations in a temperature range 30 K<T<340 K. Abrupt shifts of the experimental values reveal the structural transitions. It is seen that by taking the organic molecule fluctuations into account the calculations give a better approximation of the experimental values. The evolution of the field fluctuation rate with temperature also demonstrates the presence of molecular fluctuations as well as the onset and evolution of ion diffusion. In an illuminated environment the organic molecule fluctuations are amplified. Moreover, the structural transitions appear to be shifted at lower temperatures, meaning that they are potentially driven by molecular fluctuations. This effect would be directly demonstrated with X-ray diffraction under illumination. Furthermore, detailed measurements in the cubic phase of both crystals are needed to determine whether the reverse effect that illumination seems to have on $Br^-$ and $Cl^-$ diffusion is actually valid or not.

The results of our studies exemplify the ability of $\mu SR$ not only to probe directly and extract information on the microscopic configuration and dynamics of magnetically ordered systems but also to indirectly identify structural changes, lattice dynamics, ion kinematics and determine characteristic lengths on various systems.

# Acknowledgements

First, I would like to thank the Swedish Research Council and the Area of Advance Materials Science of Chalmers University of Technology for providing the necessary funding to carry out these studies.

I would also like to thank my supervisors, Yasmine Sassa and Lars Börjesson, for giving me the opportunity to participate in several interesting projects, explore our research field and learn new experimental methods. Your guidance and perspective has shown me paths to grow as a scientist and for that I am grateful.

To the past and present members of (K)MF, thank you for always being willing to answer all my questions and help me use our facilities. Thank you for creating a friendly and welcoming atmosphere for each one of us, with my examiner Aleksandar Matic setting such an example. Our time together, in and out of the office makes every day fuller and diverse.

A big thanks to my collaborators from KTH and CROSS with whom I have spent days and nights together during beamtimes. Your knowledge, experience and professionalism was essential in every single experiment. You gave me confidence to take responsibility in stressful times and were there whenever help was needed.

Finally, I would like to thank my partner for her endless support and understanding. My parents who always stood behind my decisions, sacrificing the time we spend together. All my friends in Sweden and Greece for all our conversations and the sense of belonging that makes all of us better people.

Konstantinos Papadopoulos, Gothenburg, May 2022

# Bibliography


[1] N. BOHR, "Atomic structure," *Nature*, vol. 107, pp. 104–107, mar 1921.

[2] E. B. Podgorsak, *Radiation Physics for Medical Physicists*. Springer-Verlag GmbH, Nov. 2016.

[3] A. Kastberg, *Structure of Multielectron Atoms*. Springer-Verlag GmbH, Apr. 2020.

[4] A. R. Pietro Carretta, *Structure of Matter*. Springer International Publishing, June 2015.

[5] G. K. Woodgate, *Elementary Atomic Structure*. OUP Oxford, Aug. 1983.

[6] N. Ashcroft, *Solid state physics*. New York: Holt, Rinehart and Winston, 1976.

[7] H. A. Bethe, "Splitting of terms in crystals," in *World Scientific Series in 20th Century Physics*, pp. 1–72, WORLD SCIENTIFIC, jul 1997.

[8] P. G. Evans and E. D. Isaacs, "Magnetic x-ray microdiffraction," *Journal of Physics D: Applied Physics*, vol. 39, pp. R245–R263, jul 2006.

[9] W. Heisenberg, "Zur theorie des ferromagnetismus," in *Original Scientific Papers Wissenschaftliche Originalarbeiten*, pp. 580–597, Springer Berlin Heidelberg, 1985.

[10] M. E. Fisher, "Magnetism in one-dimensional systems—the heisenberg model for infinite spin," *American Journal of Physics*, vol. 32, pp. 343–346, may 1964.

[11] P. W. Anderson, "New approach to the theory of superexchange interactions," *Physical Review*, vol. 115, pp. 2–13, jul 1959.

[12] J. Goodenough, *Magnetism and the chemical bond*. Huntington, N.Y: R.E. Krieger Pub. Co, 1976.

[13] D. P. Arovas, E. Berg, S. A. Kivelson, and S. Raghu, "The hubbard model," *Annual Review of Condensed Matter Physics*, vol. 13, pp. 239–274, mar 2022.

[14] P. Weiss, "L'hypothèse du champ moléculaire et la propriété ferromagnétique," *Journal de Physique Théorique et Appliquée*, vol. 6, no. 1, pp. 661–690, 1907.

[15] K. H. J. Buschow, *Handbook of Magnetic Materials: Volume 13*. NORTH HOLLAND, Apr. 2001.

[16] U. o. O. B. Stephen (Department of Physics, *Magnetism in Condensed Matter*. Oxford University Press, Oct. 2001.

[17] *Introduction to Frustrated Magnetism*. Springer Berlin Heidelberg, Jan. 2011.

[18] S. V. Streltsov and D. I. Khomskii, "Jahn-teller effect and spin-orbit coupling: Friends or foes?," *Physical Review X*, vol. 10, p. 031043, aug 2020.

[19] J. Chaloupka and A. M. Oleś, "Spin-orbital resonating valence bond liquid on a triangular lattice: Evidence from finite-cluster diagonalization," *Physical Review B*, vol. 83, p. 094406, mar 2011.

[20] G. Khaliullin and S. Maekawa, "Orbital liquid in three-dimensional mott insulator: Latio 3," *Physical review letters*, vol. 85, no. 18, p. 3950, 2000.

[21] B. Normand and A. M. Oleś, "Frustration and entanglement in the t 2 g spin-orbital model on a triangular lattice: Valence-bond and generalized liquid states," *Physical Review B*, vol. 78, no. 9, p. 094427, 2008.

[22] K. Momma and F. Izumi, "Vesta: a three-dimensional visualization system for electronic and structural analysis," *Journal of Applied crystallography*, vol. 41, no. 3, pp. 653–658, 2008.

[23] M. A. Peña and J. L. G. Fierro, "Chemical structures and performance of perovskite oxides," *Chemical Reviews*, vol. 101, pp. 1981–2018, may 2001.

[24] G. King and P. M. Woodward, "Cation ordering in perovskites," *Journal of Materials Chemistry*, vol. 20, no. 28, pp. 5785–5796, 2010.

[25] *Revolution of Perovskite: Synthesis, Properties and Applications*. SPRINGER NATURE, Jan. 2020.

[26] M. Kubicek, A. H. Bork, and J. L. M. Rupp, "Perovskite oxides – a review on a versatile material class for solar-to-fuel conversion processes," *Journal of Materials Chemistry A*, vol. 5, no. 24, pp. 11983–12000, 2017.

[27] R. J. D. Tilley, *Perovskites*. WILEY, May 2016.

[28] A. M. Glazer, "The classification of tilted octahedra in perovskites," *Acta Crystallographica Section B Structural Crystallography and Crystal Chemistry*, vol. 28, pp. 3384–3392, nov 1972.

[29] P. M. C. Rourke, I. Mouzopoulou, X. Xu, C. Panagopoulos, Y. Wang, B. Vignolle, C. Proust, E. V. Kurganova, U. Zeitler, Y. Tanabe, T. Adachi, Y. Koike, and N. E. Hussey, "Phase-fluctuating superconductivity in overdoped la2-xSrxCuO4," *Nature Physics*, vol. 7, pp. 455–458, mar 2011.

[30] J. B. Goodenough, "Electronic structure of CMR manganites (invited)," *Journal of Applied Physics*, vol. 81, pp. 5330–5335, apr 1997.

[31] B. Stojanovic, C. Jovalekic, V. Vukotic, A. Simoes, and J. A. Varela, "Ferroelectric properties of mechanically synthesized nanosized barium titanate," *Ferroelectrics*, vol. 319, no. 1, pp. 65–73, 2005.

[32] P. Muralt, R. G. Polcawich, and S. Trolier-McKinstry, "Piezoelectric thin films for sensors, actuators, and energy harvesting," *MRS bulletin*, vol. 34, no. 9, pp. 658–664, 2009.

[33] M. ANDERSON, K. GREENWOOD, G. TAYLOR, and K. POEPPELMEIER, "B-cation arrangements in double perovskites," *Progress in Solid State Chemistry*, vol. 22, no. 3, pp. 197–233, 1993.

[34] W. Bao, J. D. Axe, C. H. Chen, and S.-W. Cheong, "Impact of charge ordering on magnetic correlations in perovskite(bi,ca)MnO3," *Physical Review Letters*, vol. 78, pp. 543–546, jan 1997.

[35] D. Serrate, J. De Teresa, and M. Ibarra, "Double perovskites with ferromagnetism above room temperature," *Journal of Physics: Condensed Matter*, vol. 19, no. 2, p. 023201, 2006.

[36] J. Blasco, C. Ritter, L. Morellon, P. Algarabel, J. De Teresa, D. Serrate, J. Garcıa, and M. Ibarra, "Structural, magnetic and transport properties of sr2fe1-xcrxmoo6- y," *Solid state sciences*, vol. 4, no. 5, pp. 651–660, 2002.

[37] T.-W. Lim, S.-D. Kim, K.-D. Sung, Y.-M. Rhyim, H. Jeen, J. Yun, K.-H. Kim, K.-M. Song, S. Lee, S.-Y. Chung, M. Choi, and S.-Y. Choi, "Insights into cationic ordering in re-based double perovskite oxides," *Scientific Reports*, vol. 6, jan 2016.

[38] K. Leng, Q. Tang, Y. Wei, L. Yang, Y. Xie, Z. Wu, and X. Zhu, "Recent advances in re-based double perovskites: Synthesis, structural characterization, physical properties, advanced applications, and theoretical studies," *AIP Advances*, vol. 10, p. 120701, dec 2020.

[39] "Best research-cell efficiency chart." `https://www.nrel.gov/pv/cell-efficiency.html`. Accessed: 2022-04-29.

[40] T. Chen, W.-L. Chen, B. J. Foley, J. Lee, J. P. C. Ruff, J. Y. P. Ko, C. M. Brown, L. W. Harriger, D. Zhang, C. Park, M. Yoon, Y.-M. Chang, J. J. Choi, and S.-H. Lee, "Origin of long lifetime of band-edge charge carriers in organic–inorganic lead iodide perovskites," *Proceedings of the National Academy of Sciences*, vol. 114, pp. 7519–7524, jul 2017.

[41] D. Cui, Z. Yang, D. Yang, X. Ren, Y. Liu, Q. Wei, H. Fan, J. Zeng, and S. F. Liu, "Color-tuned perovskite films prepared for efficient solar cell applications," *The Journal of Physical Chemistry C*, vol. 120, pp. 42–47, dec 2015.

[42] P. Roy, N. K. Sinha, S. Tiwari, and A. Khare, "A review on perovskite solar cells: Evolution of architecture, fabrication techniques, commercialization issues and status," *Solar Energy*, vol. 198, pp. 665–688, mar 2020.

[43] A. Djurišić, F. Liu, H. Tam, M. Wong, A. Ng, C. Surya, W. Chen, and Z. He, "Perovskite solar cells-an overview of critical issues," *Progress in Quantum Electronics*, vol. 53, pp. 1–37, 2017.

[44] M. Bokdam, J. Lahnsteiner, and D. Sarma, "Exploring librational pathways with on-the-fly machine-learning force fields: Methylammonium molecules in mapbx3 (x= i, br, cl) perovskites," *The Journal of Physical Chemistry C*, vol. 125, no. 38, pp. 21077–21086, 2021.

[45] T. Chen, W.-L. Chen, B. J. Foley, J. Lee, J. P. Ruff, J. P. Ko, C. M. Brown, L. W. Harriger, D. Zhang, C. Park, *et al.*, "Origin of long lifetime of band-edge charge carriers in organic–inorganic lead iodide perovskites," *Proceedings of the National Academy of Sciences*, vol. 114, no. 29, pp. 7519–7524, 2017.

[46] D. Luo, R. Su, W. Zhang, Q. Gong, and R. Zhu, "Minimizing non-radiative recombination losses in perovskite solar cells," *Nature Reviews Materials*, vol. 5, pp. 44–60, nov 2019.

[47] A. Crovetto, M. K. Huss-Hansen, and O. Hansen, "How the relative permittivity of solar cell materials influences solar cell performance," *Solar Energy*, vol. 149, pp. 145–150, jun 2017.

[48] D. W. deQuilettes, S. Koch, S. Burke, R. K. Paranji, A. J. Shropshire, M. E. Ziffer, and D. S. Ginger, "Photoluminescence lifetimes exceeding 8 s and quantum yields exceeding 30% in hybrid perovskite thin films by ligand passivation," *ACS Energy Letters*, vol. 1, pp. 438–444, jul 2016.

[49] J. M. Frost and A. Walsh, "What is moving in hybrid halide perovskite solar cells?," *Accounts of Chemical Research*, vol. 49, pp. 528–535, feb 2016.

[50] R. L. Garwin, L. M. Lederman, and M. Weinrich, "Observations of the failure of conservation of parity and charge conjugation in meson decays: the magnetic moment of the free muon," *Physical Review*, vol. 105, pp. 1415–1417, feb 1957.

[51] S. J. Blundell, "Spin-polarized muons in condensed matter physics," *Contemporary Physics*, vol. 40, pp. 175–192, may 1999.

[52] P. D. De Reotier and A. Yaouanc, "Muon spin rotation and relaxation in magnetic materials," *Journal of Physics: Condensed Matter*, vol. 9, no. 43, p. 9113, 1997.

[53] A. D. Hillier, S. J. Blundell, I. McKenzie, I. Umegaki, L. Shu, J. A. Wright, T. Prokscha, F. Bert, K. Shimomura, A. Berlie, H. Alberto, and I. Watanabe, "Muon spin spectroscopy," *Nature Reviews Methods Primers*, vol. 2, jan 2022.

[54] I. A. Campbell, A. Amato, F. N. Gygax, D. Herlach, A. Schenck, R. Cywinski, and S. H. Kilcoyne, "Dynamics in canonical spin glasses observed by muon spin depolarization," *Physical Review Letters*, vol. 72, pp. 1291–1294, feb 1994.

[55] B. Rainford, R. Cywinski, and S. Dakin, "Neutron and SR studies of spin fluctuations in YMn2 and related alloys," *Journal of Magnetism and Magnetic Materials*, vol. 140-144, pp. 805–806, feb 1995.

[56] S. W. Lovesey, K. N. Trohidou, and E. B. Karlsson, "Muon spin relaxation in ferromagnets. II. critical and paramagnetic magnetization fluctuations," *Journal of Physics: Condensed Matter*, vol. 4, pp. 2061–2071, feb 1992.

[57] D. T. Adroja, S. Sharma, C. Ritter, A. D. Hillier, D. Le, C. V. Tomy, R. Singh, R. I. Smith, M. Koza, A. Sundaresan, and S. Langridge, "Muon spin rotation and neutron scattering investigations of the b -site ordered double perovskite sr2dyruo6," *Physical Review B*, vol. 101, p. 094413, mar 2020.

[58] R. Kubo and T. Toyabe, "Magnetic resonance and relaxation proc. 14th coll," *Ampère (1967)*, 1966.

[59] K. Papadopoulos, "Investigation of magnetic order in nickel-5d transition metal systems," 2019.

[60] I. McClelland, B. Johnston, P. J. Baker, M. Amores, E. J. Cussen, and S. A. Corr, "Muon spectroscopy for investigating diffusion in energy storage materials," *Annual Review of Materials Research*, vol. 50, pp. 371–393, jul 2020.

[61] J. Sugiyama, "Ion diffusion in solids probed by muon-spin spectroscopy," *Journal of the Physical Society of Japan*, vol. 82, p. SA023, jan 2013.

[62] P. Mendels, F. Bert, M. A. de Vries, A. Olariu, A. Harrison, F. Duc, J. Trombe, J. S. Lord, A. Amato, and C. Baines, "Quantum magnetism in the paratacamite family: towards an ideal kagomé lattice," *Physical review letters*, vol. 98, no. 7, p. 077204, 2007.

[63] F. L. Pratt, P. J. Baker, S. J. Blundell, T. Lancaster, S. Ohira-Kawamura, C. Baines, Y. Shimizu, K. Kanoda, I. Watanabe, and G. Saito, "Magnetic and non-magnetic phases of a quantum spin liquid," *Nature*, vol. 471, pp. 612–616, mar 2011.

[64] A. Suter, E. Morenzoni, T. Prokscha, B. M. Wojek, H. Luetkens, G. Nieuwenhuys, A. Gozar, G. Logvenov, and I. Božović, "Two-dimensional magnetic and superconducting phases in metal-InsulatorLa2-xSrxCuO4superlattices measured by muon-spin rotation," *Physical Review Letters*, vol. 106, p. 237003, jun 2011.

[65] R. Abela, F. Foroughi, and D. Renker, "Muon beams at PSI," *Zeitschrift für Physik C Particles and Fields*, vol. 56, pp. S240–S242, mar 1992.

[66] D. Arseneau, B. Hitti, S. Kreitzman, and E. Whidden *Hyperfine Interactions*, vol. 106, no. 1/4, pp. 277–282, 1997.

[67] A. Hillier, P. King, S. Cottrell, and J. Lord, "The musr user guide," *ISIS Facility, STFC, Rutherford Appleton Laboratory, UK*, 2005.

[68] S. Kilcoyne, S. Brown, S. Cottrell, S. Johnston, and C. Scott, "Musr user guide," *Unknown*, 1994.

[69] J. Sonier, "Muon spin rotation/relaxation/resonance ($\mu$sr)," *$\mu$Sr Studies Of Vortex State In Type-Ii Superconductors, Rev. Mod. Physics*, vol. 72, p. 769, 2000.

[70] J. H. Brewer, "$\mu$sr howto," *Hyperfine Interactions*, vol. 230, no. 1, pp. 35–55, 2015.

[71] A. Amato, "Physics with muons: from atomic physics to solid state physics."

[72] S. Jana, P. Aich, P. A. Kumar, O. K. Forslund, E. Nocerino, V. Pomjakushin, M. Månsson, Y. Sassa, P. Svedlindh, O. Karis, V. Siruguri, and S. Ray, "Revisiting goodenough-kanamori rules in a new series of double perovskites LaSr1-xCaxNiReO6," *Scientific Reports*, vol. 9, dec 2019.

[73] J. De Teresa, D. Serrate, J. Blasco, M. Ibarra, and L. Morellon, "Impact of cation size on magnetic properties of (a a) 2 fereo 6 double perovskites," *Physical Review B*, vol. 69, no. 14, p. 144401, 2004.

[74] P.-L. Ho, C.-P. Yu, Q. Zhang, K. Song, J. P. Buban, S.-Y. Choi, R. E. Dunin-Borkowski, J. Mayer, N.-H. Tai, J. Zhu, L. Jin, and X. Zhong, "Effect of cation ratio and order on magnetic circular dichroism in the double perovskite sr2fe1re1-o6," *Ultramicroscopy*, vol. 193, pp. 137–142, oct 2018.

[75] N. Auth, G. Jakob, W. Westerburg, C. Ritter, I. Bonn, C. Felser, and W. Tremel, "Crystal structure and magnetism of the double perovskites a2fereo6 (a=ca, sr, ba)," *Journal of Magnetism and Magnetic Materials*, vol. 272-276, pp. E607–E608, may 2004.

[76] G. Popov, M. Greenblatt, and M. Croft, "Large effects of a-site average cation size on the properties of the double perovskites ba 2- x sr x mnreo 6: A d 5- d 1 system," *Physical Review B*, vol. 67, no. 2, p. 024406, 2003.

[77] X. Ou, F. Fan, X. Chen, T. Li, L. Jiang, A. Stroppa, X. Ouyang, and H. Wu, "Magnetic frustration in double perovskite LaSrNiRuO sub6/sub," *EPL (Europhysics Letters)*, vol. 123, p. 57003, oct 2018.

[78] O. K. Forslund, K. Papadopoulos, E. Nocerino, G. Morris, B. Hitti, D. Arseneau, V. Pomjakushin, N. Matsubara, J.-C. Orain, P. Svedlindh, *et al.*, "Intertwined magnetic sublattices in the double perovskite compound lasrnireo 6," *Physical Review B*, vol. 102, no. 14, p. 144409, 2020.

[79] K. Papadopoulos, O. K. Forslund, E. Nocerino, F. O. Johansson, G. Simutis, N. Matsubara, G. Morris, B. Hitti, D. Arseneau, J.-C. Orain, *et al.*, "Influence of the magnetic sub-lattices in the double perovskite compound lacanireo6," *arXiv preprint arXiv:2111.05920*, 2021.

[80] L. Eyring, K. A. Gschneidner, and G. H. Lander, *Handbook on the physics and chemistry of rare earths*, vol. 32. Elsevier, 2002.

[81] M. I. Saidaminov, A. L. Abdelhady, B. Murali, E. Alarousu, V. M. Burlakov, W. Peng, I. Dursun, L. Wang, Y. He, G. Maculan, A. Goriely, T. Wu, O. F. Mohammed, and O. M. Bakr, "High-quality bulk hybrid perovskite single crystals within minutes by inverse temperature crystallization," *Nature Communications*, vol. 6, jul 2015.

[82] G. Maculan, A. D. Sheikh, A. L. Abdelhady, M. I. Saidaminov, M. A. Haque, B. Murali, E. Alarousu, O. F. Mohammed, T. Wu, and O. M. Bakr, "CHsub3/subNHsub3/subPbClsub3/sub single crystals: Inverse temperature crystallization and visible-blind UV-photodetector," *The Journal of Physical Chemistry Letters*, vol. 6, pp. 3781–3786, sep 2015.

[83] D. Ghosh, P. Walsh Atkins, M. S. Islam, A. B. Walker, and C. Eames, "Good vibrations: Locking of octahedral tilting in mixed-cation iodide perovskites for solar cells," *ACS Energy Letters*, vol. 2, no. 10, pp. 2424–2429, 2017.

[84] Y. Chen, H. T. Yi, X. Wu, R. Haroldson, Y. N. Gartstein, Y. I. Rodionov, K. S. Tikhonov, A. Zakhidov, X. Y. Zhu, and V. Podzorov, "Extended carrier lifetimes and diffusion in hybrid perovskites revealed by hall effect and photoconductivity measurements," *Nature Communications*, vol. 7, aug 2016.

[85] H. Zhu, K. Miyata, Y. Fu, J. Wang, P. P. Joshi, D. Niesner, K. W. Williams, S. Jin, and X.-Y. Zhu, "Screening in crystalline liquids protects energetic carriers in hybrid perovskites," *Science*, vol. 353, pp. 1409–1413, sep 2016.

[86] A. Bonadio, C. A. Escanhoela, F. P. Sabino, G. Sombrio, V. G. de Paula, F. F. Ferreira, A. Janotti, G. M. Dalpian, and J. A. Souza, "Entropy-driven stabilization of the cubic phase of MaPbIsub3/sub at room temperature," *Journal of Materials Chemistry A*, vol. 9, no. 2, pp. 1089–1099, 2021.

[87] K.-H. Wang, L.-C. Li, M. Shellaiah, and K. W. Sun, "Structural and photophysical properties of methylammonium lead tribromide (MAPbBr3) single crystals," *Scientific Reports*, vol. 7, oct 2017.

[88] H.-P. Hsu, L.-C. Li, M. Shellaiah, and K. W. Sun, "Structural, photophysical, and electronic properties of CH3nh3pbcl3 single crystals," *Scientific Reports*, vol. 9, sep 2019.